Inorganic Chemistry

Article

pubs.acs.org/IC

Enhanced Catalytic Activity of Zeolite Encapsulated Fe(III)-Schiff-Base Complexes for Oxidative Coupling of 2-Napthol

Kusum K. Bania,[†] Dipsikha Bharali,[†] B. Viswanathan,[‡] and Ramesh C. Deka*[,†]

[†]Department of Chemical Sciences, Tezpur University, Napaam, Tezpur—784 028, Assam, India

[‡]Department of Chemistry, Indian Institute of Technology, Madras, Chennai—600 036, India

Supporting Information

ABSTRACT: Iron(III) Schiff-base complexes of general formula $[Fe(L)_2Cl]\cdot 2H_2O$, where L = *N*,*Ń*-bis(salicylidene)-ethylenediamine and *N*,*Ń*-disalicylidene-1,2-phenylenediamine have been encapsulated within various alkali exchanged zeolites viz. LiY, NaY, and KY by flexible ligand method. The encapsulated complexes are characterized by EDX, scanning electron microscopy (SEM), powder X-ray diffraction (XRD), FT-IR, UV−vis, diffuse reflectance spectroscopy (DRS), electron spin resonance spectroscopy (ESR) and cyclic voltammetry studies. The diffuse reflectance UV−vis spectra of encapsulated complexes show a dramatic red shift of the charge transfer band with increasing electropositivity of the exchangeable cations. The electrochemical analysis predicts the shifting of the reduction potential toward negative values with increasing size of the alkali exchanged cations. The zeolite encapsulated Schiff-base complexes of iron are found to be catalytically active toward the oxidative coupling of 2-napthol. Metal complexes incorporated in potassium exchanged zeolite-Y are found to be more effective for catalytic conversion of 2-naphthol to binaphthol and induces higher selectivity toward the *R*-conformation. The catalytic conversion of 2-napthol to BINOL is found to depend on the reduction potential of the catalyst, with a more negative reduction potential being better for the catalytic conversion. Density functional calculation is being carried out on both the neat Fe-Salen and Fe-Salophen complexes and those encapsulated in NaY zeolite to investigate change in structural parameters, energies of the HOMO and LUMO, and global hardness and softness. Fukui functions, as local descriptors, are used to analyze the hard−hard interaction at a particular site of the complexes.

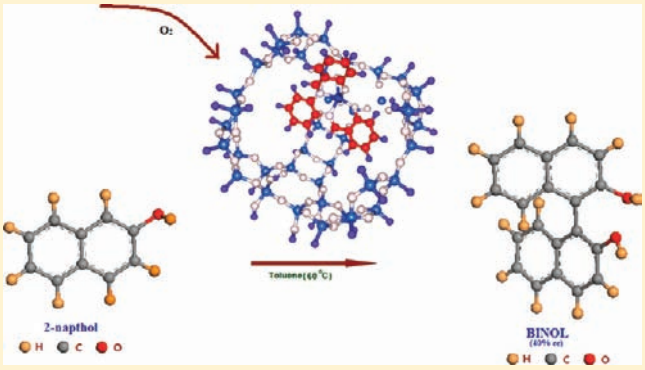

1. INTRODUCTION

Zeolites are attractive materials for encapsulation of transition metal complexes, organometallics, organic dyes, and polymers within their voids.[1−3] The topology of the voids and the steric and electrostatic constraints imposed by the walls of the zeolite framework can influence the geometry and hence change magnetic, electronic, and redox properties of the encapsulated complex, leading to changes in the reactivity of the enclosed species.[4,5] Besides the space and steric constraints of the zeolite matrix, the cations in zeolites have been known to play an important role other than merely compensating the negative charge in the framework. It has been shown that the cations govern the donor strength of the zeolite framework and the strength increases with increasing electropositivity of the cations.[6,7] Physicochemical characteristics such as electrostatic potential and electric field within the cage, spin−orbit parameter, and space available for guest molecules within the supercage are known to be controlled by these exchangeable charge compensating alkali metal cations. Moreover, one can readily switch to a base catalyst by replacing Na^+ of zeolite-NaY with other large alkali metal cations such as Cs^+.[8,9] It has also been reported that these cations offer different reactive sites for the interaction of the incoming guest molecules.[10,11] However, only a limited number of studies have been addressed to examine the effect of alkali metal cations on the physicochemical, electronic, redox, and catalytic behavior of zeolite encapsulated transition metal complexes.[12,13]

The zeolite encapsulated transition metal complexes of Shiff-base ligands especially of Salen are well-known to mimic the catalytic cycle of cytochrome P-450 and have attracted research interest in recent years.[14,15] They have been extensively used as biomimetic catalysts for hydrocarbon hydroxylation/epoxidation and alcohol carbonylation with a variety of oxidants including hydrogen peroxide,[16−20] tertbutylhydroperoxide (TBHP),[14,20,22] and iodosylbenzenes (PhIO)[20,23] and with less frequent use of O_2 as oxidant.[24,25] Molecular oxygen is not considered to be a good oxidant as compared to other oxidants mentioned for oxidation reaction of organic substrates because of its higher chemical stability. So, the search for a better catalyst which can reduce molecular oxygen and thus make use of it as oxidant in organic reaction is ongoing. It has been

Received: September 7, 2011
Published: January 18, 2012

   dx.doi.org/10.1021/ic201959g | *Inorg. Chem.* 2012, 51, 1657−1674

reported on the basis of electrochemical studies that Schiff-base complexes of Fe, Mn, and Co encapsulated in zeolite-Y can reduce the molecular oxygen to water.[26]

Asymmetric aerobic oxidative coupling of 2-napthol to BINOL is now considered to be the most atom economical method but limited successes have been obtained by the extension of the known homocoupling reaction. Since C_1- and C_2-symmetric BINOL and its derivative are deemed to be efficient chiral auxiliaries, design of newer catalysts for such oxidative coupling reaction is now under development. Also, recent studies have shown that the chiral iron(Salen) complex can act as a better catalyst for aerobic oxidative coupling of 2-napthol.[27,28] However, the catalytic activity of achiral Fe(Schiff) base complexes without any additive are less explored in such a kind of oxidative coupling reaction since they are less facile in bringing out the enantioselectivity in the resultant BINOL.

Stemming from our interest in the effect of alkali metal cations on the physicochemical properties and reactivity of encapsulated transition metal complexes, in this work we have carried out a systematic study on the effect of countercations of zeolite on the charge transfer bands of Fe-Schiff-base complexes (Fe-Salen and Fe-Salophen) encapsulated in zeolite-Y and its synergistic effect on the redox potential of the encapsulated complexes. Also, we tried to shed light on dependency of the aerobic oxidative coupling of 2-napthol on the redox potential of the catalyst and rationalize how the size of the alkali metal cations controls the chirality inside the confined space of zeolite. Density functional theory (DFT) methods have been extensively used to understand the structure, electronic properties, and chemical reactivity of zeolitic materials.[29]

2. EXPERIMENTAL METHOD

2.1. Materials and Physical Measurements. NaY zeolites are purchased from HiMedia India Pvt. Ltd. The chemicals used for the synthesis of iron Schiff-base complexes are anhydrous ferric chloride (Otto kemi) salicylaldehyde (Merck), *o*-phenylenediamine CDH (Central Drug House), and ethylenediamine (Merck). For the preparation of alkali exchanged zeolites we used lithium chloride and potassium nitrate (Rankem). 2-Naphthol [analytical grade (AR), G.S Chemical Testing Lab & Allied Industries, Bombay] is used in the oxidative coupling reaction. All the solvents (dimethylformamide, diethyl ether, ethyl alcohol, methanol, acetone, and toluene) are purified prior to use. Powder X-ray diffraction (XRD) patterns are recorded on a Shimadzu XD-D1 powder X-ray diffractometer using Cu Kα radiation (λ = 1.542 Å). XRD patterns are recorded in the 2θ range 5−50° at a scanning rate of 2°/min. The electronic absorption spectra are recorded using a Hitachi U-3400 spectrophotometer with a diffuse reflectance attachment equipped with an integrating sphere of 60 mm inner diameter. Monochromatic light was used in the whole spectral region in order to minimize the effect of fluorescence. For recording the spectra of the cation exchanged zeolites and zeolite encapsulated metal complexes, the powdered samples are placed in a black absorbing hole (10 mm, in diameter, and 3 mm deep) of a sample holder, and the surface is smoothed. The layer can be regarded as infinitely thick, as required by the Kubelka−Munk theory. The optical spectra are then recorded in the reflectance mode. A Kubelka−Munk (KM) analysis[30] is performed on the reflectance data. The KM factor, $F(R)$, is given by $F(R) = (1 - R)^2/2R = k/s$ where R is the diffuse reflectance of the sample as compared to $BaSO_4$, k is the molar absorption coefficient, and s is the scattering coefficient of the sample. The infrared spectra in the range 450−4000 cm^{-1} are recorded on a Perkin-Elmer Spectrum 2000 FTIR spectrometer using a DRIFT accessory. The spectra of the neat Fe-Schiff-base complexes and the zeolite-encapsulated complexes are recorded as KBr pellets by mixing the samples well with KBr in 1:100 ratios. Electron spin resonance (ESR) spectra of neat complexes are recorded in appropriate solvents with a Varian E-112 spectrometer at liquid nitrogen temperature (77 K). The SEM and elemental chemical analyses are performed by using JEOL JSM-6390 LV at an acceleration voltage of 5−10 kV. The samples are deposited on a brass holder and sputtered with platinum. Thermogravimetric and differential thermal analysis are performed on simultaneous TG-DTA thermoanalyzer, Mettler Toledo, with a Pt crucible, Pt/Pt−Rh 13% thermocouples, and flow rate of the controlling gas (air) of 20 mL/min. The cyclic voltammograms of neat and encapsulated complexes are recorded on a Wenking potentioscan (model POS73) with a digital recorder, and 0.1 M TBAP is used as the supporting electrolyte. The working electrode is prepared by taking a 1:1 weight ratio of neat or encapsulated metal complexes in 1 mL of DCM. This suspension is ultrasonicated for 15 min. A 10 μL sample of this dispersion is coated on glassy carbon electrode, and 5 μL of 5% styrene (as binder from Aldrich) is added to these coatings and dried. The glassy carbon electrode is used as the working electrode and Ag/AgCl/KCl (saturated) is used as reference electrode. The cyclic voltammograms of neat complexes are taken in solution mode, using 0.01 M of the metal complexes in a 0.1 M tetra-butyl-ammonium phosphate (TBAP). Cyclic voltammograms of all the catalysts are taken in 10 mL of DCM using 0.1 M TBAP as supporting electrolyte.

2.2. Preparation of Schiff-Base Ligands. *2.2.1. Synthesis of N,N′-Bis(salicylidene)ethylenediamine (Salen).* To 40 mmol of salicylaldehyde (4.17 mL) 20 mmol of ethylenediamine (1.33 mL) is added under cold conditions. A yellow crystalline product so obtained after a few minutes is further recrystallized in toluene. The purity and structure of the compound are analyzed by NMR, FT-IR, and UV−vis techniques.

2.2.2. Synthesis of N,N′-Disalicylidene-1,2-phenylendiamine (Salophen). To a well-stirred solution of 10 mmol of *o*-phenylenediamine (1.08 g) in ethanol 20 mmol of salicylaldehyde (2.1 mL) is added. The mixture is stirred under reflux at 50 °C for 2 h. A yellowish orange crystalline product is obtained which is further recrystallized in toluene and analyzed by NMR, FT-IR, and UV−vis techniques.

2.3. Preparation of Fe(III) Schiff-Base Complexes. *2.3.1. Synthesis of Fe(III) Salen Complex (Complex 1).* To a well stirred solution of 1 mmol of *N,N′*-bis(salicylidene)ethylenediamine (0.268 g) in DMF (dimethylformamide) 1 mmol of $FeCl_3$ anhydrous (0.162 g) is added. The homogeneous solution is stirred for 6 h and kept for crystallization. The black crystal so obtained is washed with ethanol and diethyl ether and finally dried at room temperature.

2.3.2. Synthesis of Fe(III) Salophen Complex (Complex 2). The same procedure is carried out for the synthesis of this complex. The only difference is in the use of the ligand *N,N′*-disalicylidene-1,2-phenylendiamine instead of *N,N′*-bis(salicylidene)ethylenediamine.

2.4. Preparation of Alkali Metal Exchanged Zeolites. For the preparation of the alkali exchanged zeolite the NaY zeolite is used as precursor. The Na form of zeolite Y is treated with aqueous 1 M NaCl solution once again and subsequently washed with distilled water until the silver ion test for chloride is negative. A mixture of 2.0 g of NaY and 1 mmol (0.423 g) of LiCl in demineralized water is then stirred under reflux at 120 °C for 24 h. The slurry is then filtered and washed with distilled water and dried overnight in an oven to get Li-exchanged zeolite (Li−Y). The K−Y is obtained by exchanging NaY with 1 mmol (0.101 g) of KNO_3.

2.5. Preparation of Fe(III) Exchanged Zeolites. A mixture of 1 g of the alkali metal exchanged zeolites (LiY, NaY, and KY) and 1 mmol (0.162 g) of anhydrous $FeCl_3$ solution in water is stirred under reflux at 120 °C for 24 h. The pH of the solution is maintained within 3−3.5 using buffer tablets within that range in order to prevent the precipitation of ferric ion as $Fe(OH)_3$. The slurry is then filtered, washed with distilled water, and dried overnight in an oven at 500−550 °C to get Fe-exchanged LiY, NaY, and KY as pale yellow powder.

2.6. Encapsulation of Fe(III) Schiff-Base Complexes in Various Alkali Exchanged Zeolite-Y. The Fe^{3+} exchanged zeolites (Fe-LiY, Fe-NaY, and Fe-KY) are treated with stoichoimetric excess of *N,N′*-bis(salicylidene)ethylenediamine or *N,N′*-disalicylidene-1,2-phenylendiamine in either case. The mixture is refluxed for 48 h at 250−270 °C under constant stirring. On heating, the solid mass changed color from brownish yellow to brownish black. The zeolites are then

dx.doi.org/10.1021/ic201959g | Inorg. Chem. 2012, 51, 1657−1674

Table 1. Elemental Analyses for Pure NaY, Iron Exchanged Zeolites, and Zeolite Encapsulated Complexes

sample	metal %	Si %	Al %	alkali metal cation%	C %	H %	N%	unit cell formula
Li Y		22.76	8.60	4.85 (Li)				$Li_{34}Na_{18}[(AlO_2)_{52}(SiO_2)_{140}]$
Na Y		23.70	8.57	8.55 (Na)				$Na_{52}[(AlO_2)_{52}(SiO_2)_{140}]$
K Y		22.53	8.52	4.56 (K)				$K_{32.5}Na_{19.5}[(AlO_2)_{52}(SiO_2)_{140}]$
Li Fe Y	4.12	22.96	8.44	4.50 (Li)				$Li_{31.47}Na_{6.7}Fe_{13.8}[(AlO_2)_{52}(SiO_2)_{140}]$
Na Fe Y	4.12	22.96	8.44	5.64 (Na)				$Na_{38.4}Fe_{13.6}[(SiO_2)_{52}(AlO_2)_{140}]$
K Fe Y	4.12	22.96	8.44	4.35 (K)				$K_{30.96}Na_{5.4}Fe_{15.7}[(SiO_2)_{52}(AlO_2)_{140}]$
Fe-Salen-Li Y	1.72	21.80	8.20	3.34 (Li)	2.86	1.40	1.68	
Fe-Salen-Na Y	1.68	20.40	7.80	3.63 (Na)	2.62	1.61	1.76	
Fe-Salen-K Y	1.78	20.48	8.85	3.80 (K)	2.82	1.42	1.38	
Fe-Salophen-Li Y	1.74	21.75	8.35	3.25 (Li)	4.20	1.21	1.43	
Fe-Salophen-Na Y	1.65	21.25	8.80	3.29 (Na)	3.92	1.38	1.32	
Fe-Salophen-K Y	1.76	21.43	8.28	3.64 (K)	3.86	1.38	1.42	

filtered, washed repeatedly with deionized water, and dried at room temperature under vacuum. The resultant products are further purified by Soxhlet extraction using the sequence of solvents acetone, methanol, and finally diethyl ether to remove any unreacted species or species adsorbed on the surface of the zeolite crystallites. The products are dried under vacuum and finally kept in a muffle furnace for 48 h at 550 °C to obtain anhydous $[Fe(Salen)_2]^{3+}$ or $[Fe(Salophn)_2]^{3+}$ encapsulated NaY (Fe-Salen-NaY, Fe-Salophn-NaY), LiY (Fe-Salen-LiY, Fe-Salphn-LiY), and KY (Fe-Salen-KY, Fe salophn-KY) as reddish-brown powders.

2.7. Catalytic Oxidation of 2-Napthol. The oxidation of 2-napthol with air was carried out in a batch reactor. In a typical run, 5 mmol of 2-napthol along with 10 mL of toluene and 10 mg of catalyst are added into a 100 mL two-necked flask equipped with a condenser and an air pump. The reaction is started by bubbling the dry air with a stable flow rate of 80 mL/min controlled by a flowmeter into the bottom of reactor at reaction temperature. The progress of the reaction is monitored by thin layer chromatography, and after the completion of the reaction, the catalyst is filtered, washed with toluene, and dried at 100 °C overnight. The amount of iron content in 10 mg of the catalyst is determined according to Vogel's method.[31] The turnover number is determined by the following equation: TON = [BINOL(mmol)/ Fe-atoms on catalyst(mmol)].

2.8. Computational Method. All the density functional calculations are carried out using the DMol^3 program[32] with VWN correlation functional and double numeric (DN) basis set. We performed all electron calculations on both the neat and encapsulated iron Schiff-base complexes. The zeolite cluster is generated by taking 40 tetrahedral units (40T) of faujasite structure around the supercage, saturating them with hydrogen atoms. Initially, the framework Si and O atoms of the clusters are held fixed at their crystallographic positions, and all the terminal H atoms are optimized. Following Löwenstein's rule, three silicon atoms of the six-membered ring are replaced with three aluminum atoms. The gas phase optimized iron complexes are then encapsulated inside the supercage at several orientations. The three negative charges generated in the cluster are compensated by the three positive charges of the complex. While optimizing the clusters, terminated hydrogen atoms are held fixed at their initially optimized positions. The most stable structure is considered for further analysis. The interaction energy values between various alkali metal cation and 2-napthol are also calculated at the same level of theory. We calculated the global hardness, $\eta = {}^1/_2(E_{LUMO} - E_{HOMO})$, using Koopmans' theorem and global softness ($S = {}^1/_2\eta$) as the inverse of the global hardness, for the neat and zeolite encapsulated $[Fe(Salen)_2]^{3+}$ and $[Fe(Salophn)_2]^{3+}$ complexes. The Fukui function[33] is defined by

$$f(r) = \left[\frac{\delta^2 E}{\delta\nu(r)\delta N}\right] = \left[\frac{\delta}{\delta\nu(r)}\right]_N = \left[\frac{\delta\rho(r)}{\delta N}\right]_\nu$$

where μ is the chemical potential, $\rho(r)$ is total charge density, $\upsilon(r)$ is external potential, and N is the total number of electrons. Due to discontinuity in the $\rho(r)$ versus N curve, one can define three different types of Fukui functions, viz

$$f_k^{+} = [q_k(N+1) - q_k(N)] \text{ (for nucleophilic attack)}$$

$$f_k^{-} = [q_k(N) - q_k(N-1)] \text{ (for electrophillic attack)}$$

$$f_k^{0} = [q_k(N+1) - q_k(N-1)]/2 \text{ (for radical attack)}$$

where $q_k(N)$, $q_k(N+1)$, and $q_k(N-1)$ are the charges of the kth atom for N, $N+1$, and $N-1$ electron systems, respectively.

3. RESULTS AND DISCUSSION

3.1. Experimental Section. *3.1.1. Elemental Analysis.* The results of the elemental analyses are given in Table 1 and give Si/Al ratio of 2.76 which corresponds to a unit cell formula $Na_{52}[(AlO_2)_{52}(SiO_2)_{140}]$ for parent NaY. Despite repetition of the exchange procedure five times, elemental analysis of the final zeolites revealed incomplete exchange of alkali cations, as shown in Table 1. However, the Si/Al ratio has remained unchanged in all metal-exchanged zeolites, indicating the absence of dealumination during the exchange process. The amounts of metal content in the intrazeolite complexes are found to be less compared to the iron-exchanged zeolites. The decrease in the metal content during complex formation inside the zeolite cavity can be attributed to the participation of metal ion in the formation of coordination complexes inside the cavities of zeolite-Y, or it may so happen that some of the metal ion leaches out during complex formation.

3.1.2. X-ray Diffraction Studies. The powder X-ray diffraction patterns of the zeolite NaY, Fe^{3+} exchanged zeolites, and the encapsulated Fe-Schiff-base complexes in various alkali exchanged zeolites are shown in Figure 1. Essentially similar diffraction patterns are noticed in the encapsulated Fe-Salen (or Fe-Salophen) and NaY, except the zeolite with encapsulated Fe-Salen (or Fe-Salophen) has slightly weaker intensity. These observations indicate that the framework of the zeolite does not suffer any significant structural changes during encapsulation. However, there are differences in the relative peak intensities of the 220 and 311 reflections appearing at $2\theta = 10°$ and 12°, respectively. For pure zeolite-Y and for Fe-exchanged zeolite-Y $I_{220} > I_{311}$, but for the encapsulated complex $I_{311} > I_{220}$. This reversal in intensities has been observed more as the size of the cations increases (Li < Na < K) in encapsulated complexes (Figure 2) and has been empirically correlated with the presence of a large complex within the zeolite-Y supercage.[34] This change in the relative intensities may be associated with the redistribution of randomly coordinated free cations in

dx.doi.org/10.1021/ic201959g | Inorg. Chem. 2012, 51, 1657−1674

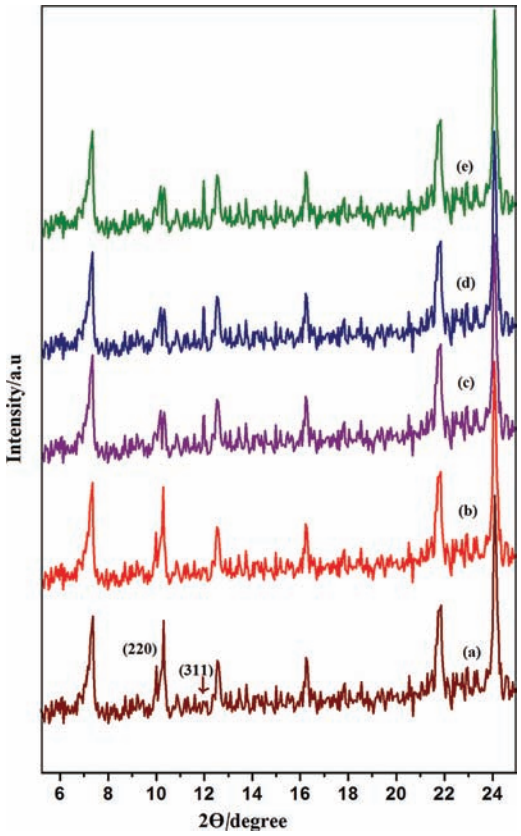

Figure 1. XRD pattern of (a) pure zeolite-Y, (b) Fe exchanged zeolite-Y, (c) Fe-Salen-LiY or Fe-Salophen-LiY, (d) Fe-Salen-NaY or Fe-Salophen-NaY, (e) Fe-Salen-KY or Fe-Salophen-KY.

zeolite Y at sites II and I. The above observation may therefore be construed as evidence for the successful encapsulation of Fe(Salen) or Fe(Salophen) complex within the supercage of zeolite Y.

3.1.3. Infrared Spectroscopy (FTIR). The FTIR spectra of NaY, Fe^{3+} exchanged zeolite-Y, and encapsulated Fe-complexes are shown in Figure 3. IR spectra of NaY and metal-exchanged zeolites show strong zeolite lattice bands in the range 450−1200 cm^{-1}. The strong and broad band at the region 1000 cm^{-1} could be attributed to the asymmetric stretching vibrations of $(Si/Al)O_4$ units. The broad bands in the region 1650 and 3500 cm^{-1} are due to lattice water molecules and surface hydroxylic groups, respectively. The parent NaY zeolite shows characteristic bands at 573, 710, 786, and 1040 cm^{-1} (Figure 3a) and are attributed to T−O bending mode, double ring, symmetric stretching, and antisymmetric vibrations, respectively.[35] These bands are not modified during the ionic exchange with alkali metal cation, Fe^{3+}, or by supporting the iron complexes (Figure 3b), which further implies that the zeolite framework has remained unchanged upon encapsulation of complexes. The IR bands of all encapsulated complexes are weak due to their low concentration in the zeolite cage and thus can only absorb in the region where the zeolite matrix does not show any absorption band that lies in the 1200−1600 cm^{-1} region. The FT-IR spectra of the ligands are provided in Supporting Information, Figure S1. The IR spectra of the neat Fe-Salen complex (Figure 3c) show major bands at 1626 (C═C), 1534, 1430 (C═N), 1288 (C−O), 1378, 767 cm^{-1} (ν_{C-H} aromatic ring), and IR spectra of the Fe-Salophen complex (Figure 3d) show major bands at 1632 (C═C), 1463, (C═N), 1302 (C−O), 1378, 751 (ν_{C-H} aromatic ring). Similar frequencies are also observed in the case of encapsulated complexes in various zeolites with a little shift in the C═N and C−O bands to wavenumbers 1522, 1450, and 1273 cm^{-1}, respectively, indicating nitrogen and oxygen coordination inside the cavity of the zeolite framework. The $\nu_{C-H\ def}$ band at 1378 cm^{-1} is shifted toward lower wavenumber as the size of the alkali cation increases. This shift in the ν_{C-Hdef} band on encapsulation has been reported for encapsulation of metal complexes in various zeolites.[36] The peak values in wavenumber of the selected IR bands for the neat and the encapsulated complexes are given in Table 2. This gives an indication for the formation of Fe Schiff-base complexes that are indeed present in the cavity of the zeolite-Y.

3.1.4. UV−Vis Spectra. The peak values for the electronic transitions observed in uncomplexed ligands, neat Fe-Schiff-base complexes, and encapsulated Fe-complexes in various alkali exchanged zeolites are given in Table 3. The absorption spectrum of uncomplexed Salen features two higher energy bands at 256 and 213 nm and two lower energy bands at 397 and 320 nm (Figure 4a). The bands at lower wavelength are attributable to $\pi \rightarrow \pi^*$ transitions, and the bands at higher wavelength arise from $n \rightarrow \pi^*$ transitions. In the corresponding phenyl substituted ligand, Salophen, absorption bands are observed at 205, 257, and 329 nm (Figure 4b). The first two bands are assigned to $\pi \rightarrow \pi^*$, and the band at 329 nm is due to $n \rightarrow \pi^*$ transition.

The Fe(III)-Salen complex in methanol solution exhibits four absorption peaks at 215, 231, 257, and 299 nm due to intra-ligand $\pi \rightarrow \pi^*$ transitions. These bands are approximately shifted relative to those of the uncomplexed ligand, Figure 4c.

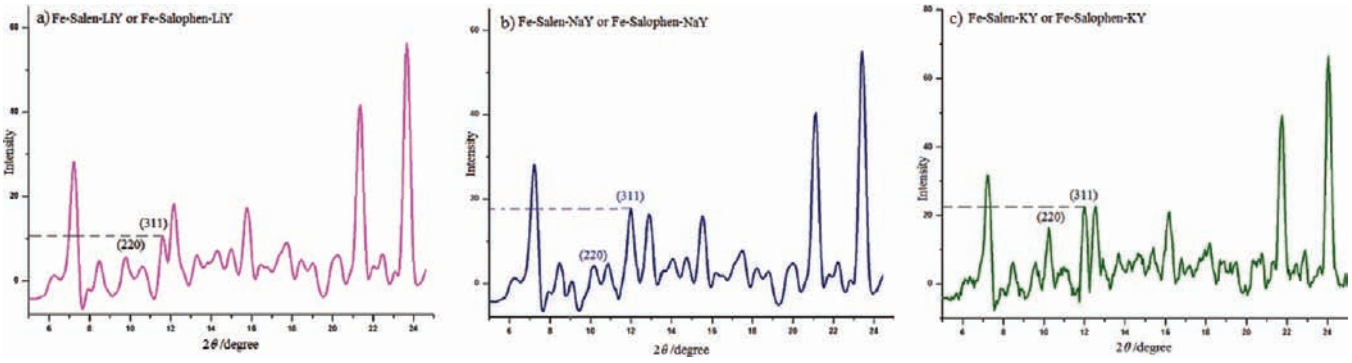

Figure 2. XRD pattern of (a) Fe-Salen-LiY or Fe-Salophen-LiY, (b) Fe-Salen-NaY or Fe-Salophen-NaY, (c) Fe-Salen-KY or Fe-Salophen-KY showing the change in intensities of 311 plane on increasing the size of alkali metal cations.

dx.doi.org/10.1021/ic201959g | Inorg. Chem. 2012, 51, 1657−1674

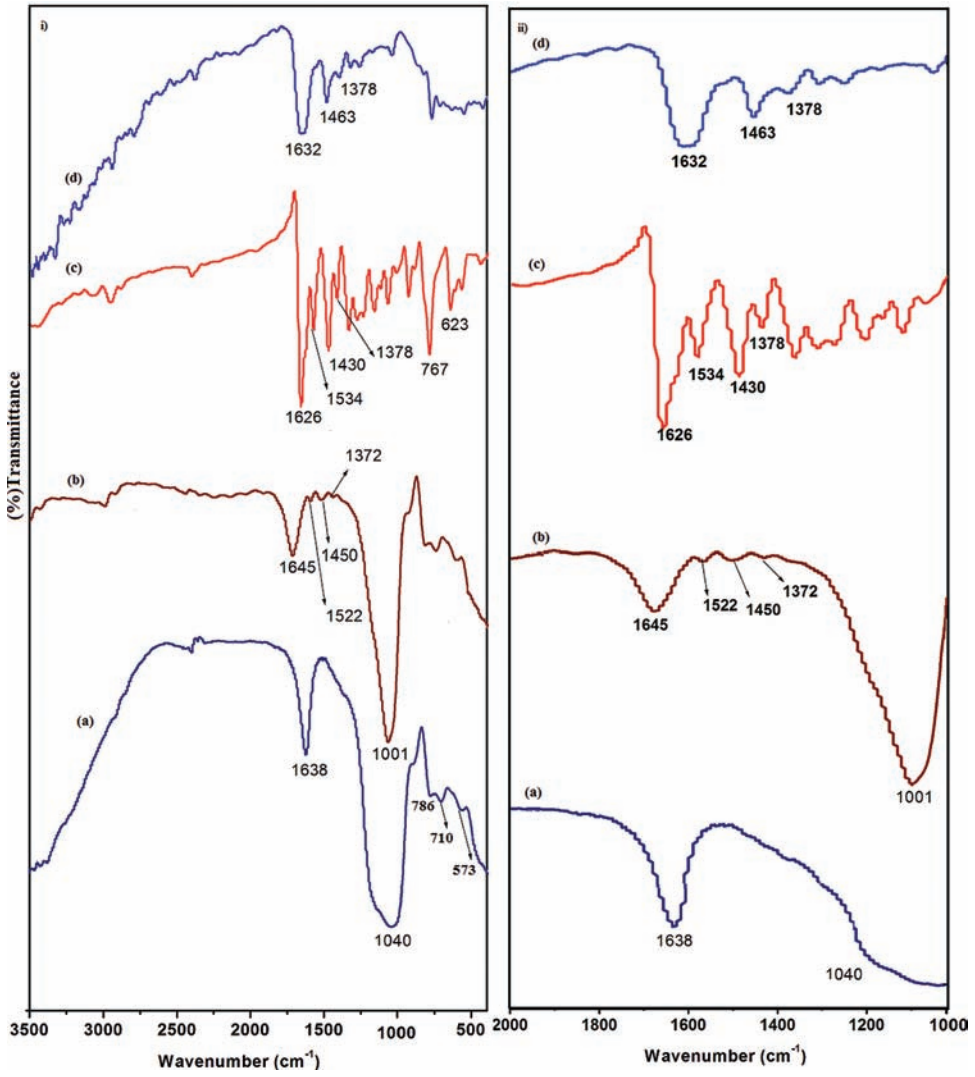

Figure 3. (i) (a) IR spectra of pure zeoliteY, (b) typical FTIR spectra of encapsulated iron Schiff-base complexes in various alkali exchanged zeolites, (c) neat Fe-Salen complex, (d) Fe-Salophen complex; (ii) expanded IR-spectrum of a–d in between 2000 and 900 cm^{-1}.

Table 2. FTIR Spectral Data (in cm^{-1}) for the Neat and the Encapsulated Fe-Schiff-Base Complexes

sample	$\nu_{C=C}$	$\nu_{C=N}$	$\nu_{C-H\ def}$	ν_{C-O}
Na Y				
Fe-Salen	1626	1534, 1430	1378, 767	1288
Fe-Salophen	1632	1463	1378, 751	1302
Fe-Salen-LiY	1645	1522, 1450	1372	1273
Fe-Salen-NaY	1644	1522, 1450	1367	1273
Fe-Salen-KY	1645	1522, 1450	1362	1273
Fe-Salophen-LiY	1645	1476	1373	1282
Fe-Salophen-NaY	1645	1476	1361	1282
Fe-Salophen-KY	1645	1476	1358	1282

Table 3. UV–Vis/DRS Spectral Data (λ_{max} in nm) for the Uncomplexed Ligands and Neat and Encapsulated Fe-Schiff-Base Complexes

	electronic transitions		
sample	$\pi \rightarrow \pi^*$	$n \rightarrow \pi^*$	$p\pi \rightarrow d\pi^*$
Salen	213, 256	320, 397	
Salophen	205, 257	329	
Fe-Salen	215, 231, 257, 299	317	505
Fe-Salophen	218, 241, 290	321	590
Fe-Salen-LiY	234, 290	427	489
Fe-Salen-NaY	237, 294	434	517
Fe-Salen-KY	239, 296	443	527
Fe-Salophen-LiY	217, 285, 317		510
Fe-Salophen-NaY	219, 287, 319		523
Fe-Salophen-KY	223, 288, 321		574

In the corresponding Fe(III)-Salophen complex, three bands are observed at 218, 241, and 290 nm as shown in Figure 4d. In addition to these $\pi \rightarrow \pi^*$ transitions two additional bands are observed in both complexes. The bands at 317 nm in the case of complex **1** and bands at 321 nm in the case of complex **2** are attributable to $n \rightarrow \pi^*$ intraligand transitions in the aromatic rings. The presence of an additional band at about 300 nm in both complexes may be due to the first allowed $\pi \rightarrow \pi^*$ transition in the aromatic rings. The most important feature in the near-UV region of the Fe(III) Schiff-base complexes is a band at 505 nm in complex **1** and weak band at 590 nm in complex **2**. These bands indicate the coordination of metal ion with the ligands, and this can be assigned to a charge-transfer band, a transition from $p\pi$ orbitals on the phenolate oxygen atom to the half-filled $d\pi^*$ orbitals of the Fe(III).[37]

dx.doi.org/10.1021/ic201959g | Inorg. Chem. 2012, 51, 1657–1674

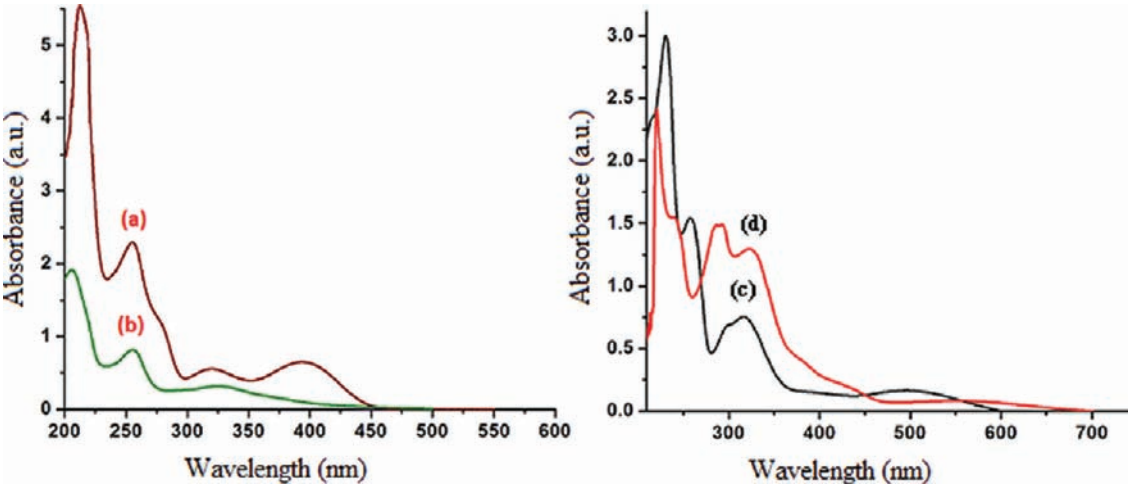

Figure 4. UV−vis spectra of (a) *N,N′*-bis(salicylidene)ethylenediamine (Salen), (b) *N,N′*-disalicylidene-1,2-phenylendiamine (Salophen), (c) neat Fe-Salen complex, and (d) neat Fe-Salophen complex.

The diffuse reflectance (DR) spectra of the dried cation exchange zeolites viz. Fe-LiY, Fe-NaY, and Fe-KY are shown in Figure 5. The DR spectrum contains an intense band at 275 nm,

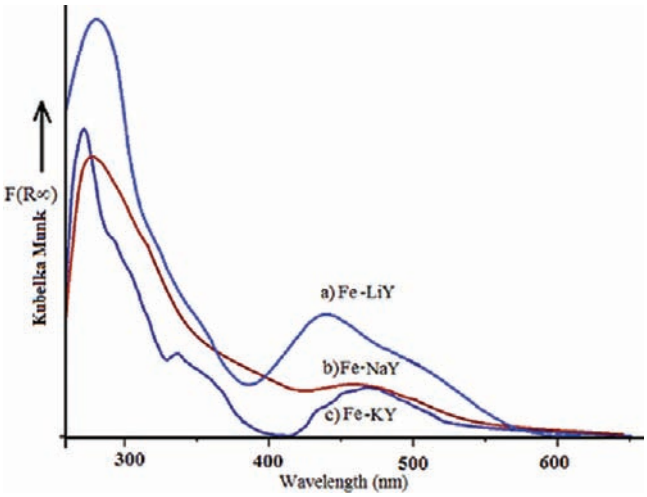

Figure 5. DR spectra of ion exchanged zeolites (a) Fe-LiY, (b) Fe-NaY, (c) Fe-KY.

a weak band at 340 nm, and a broad band in the region 420−475 nm. The low intense broad peak below 500 nm can be attributed to a ligand-to-metal charge transfer transition, in the present case from the oxygen ligand to a tetracoordinated Fe^{3+} ion. The weak bands between 300 and 400 nm may be due to formation of some iron oxide on the surface during calcination, while the peaks below 300 nm are due to isolated Fe^{3+} ions.[38−40] These results indicate that, in the dried sample, iron is mainly in the form of the Fe^{3+} ion. It can be observed from Figure 5 that on increasing the size of the alkali cation the band below 300 nm shifted to lower wavelength while the lower energy band below 500 nm shifted to higher wavelength. This further indicates that the size of the alkali metal cation influences the charge transfer transitions.

The diffuse reflectance UV−vis spectra (DRS) of the encapsulated complexes (Figure 6) show characteristic changes in electronic transitions. In the case of the Fe(III)-Salen complex encapsulated in various ion-exchanged zeolites, viz., LiY, NaY, and KY, the diffuse reflectance spectra show four major bands in the region 234, 290, 425−443, and 489−527 nm. The first two higher energy bands due to $\pi \rightarrow \pi^*$ transitions get blue-shifted in comparison to those of the neat complex. The bands below and above 480 nm are due to $n \rightarrow \pi^*$ and ligand to metal charge transfer (LMCT) transitions, respectively. Most notably, both the $n \rightarrow \pi^*$ and the charge transfer transitions are progressively red-shifted, and the intensity of the $n \rightarrow \pi^*$ gets diminished with increase in cationic size in the order Li < Na < K (Figure 6a−c). Concomitantly, the width of the charge transfer bands increases with the increase in the size of the alkali metal cation, the order being Li < Na < K. The shifting of the peak to the lower energy side in comparison to the neat complex suggests that after encapsulation the energy levels of the Fe-Salen complexes split from the barycenter under the influence of the zeolite framework, changes crystal field stabilization energy, and hence becomes less stable under the steric and space constraints imposed by the walls of the zeolite framework. A similar kind of influence of alkali metal cation on the charge transfer bands of methyl viologen and iron and ruthenium tris-(bipyridyl) complexes is reported by various authors, and this type of shifting of lower and higher energy bands has been correlated with donor strength of the zeolite framework and Sanderson's electronegativity or partial charge of the framework oxygen.[11,12,41]

The DRS of the Fe(III) Salophen complex encapsulated in various alkali-metal-cation-exchanged zeolites also shows four characteristic bands at 219, 285, 317, and 510−574 nm. The bands due to $\pi \rightarrow \pi^*$ transitions are red-shifted, and the LMCT band above 500 nm is blue-shifted corresponding to that of the neat complex. The shifting of the peak to the lower energy side when the Fe-Salophen complexes are encapsulated in zeolite-Y (Figure 6d−f) suggests a greater stability of the complexes on encapsulation inside the supercages of zeolite-Y. The possible explanations for the shifting of the peaks and significant broadening of the $p\pi \rightarrow d\pi^*$ transition bands are the following: (i) the ligands are distorted to some extent by the steric constraint imposed by the zeolite supercage, (ii) the ground and/or excited state of the LMCT transition is altered by encapsulation of Fe-Schiff-base complexes, (iii) the increase in size of alkali metal cation could mask the $n \rightarrow \pi^*$ and $p\pi \rightarrow d\pi^*$ transition, (iv) the increase in the electropositivity of the surrounding

dx.doi.org/10.1021/ic201959g | *Inorg. Chem.* 2012, 51, 1657−1674

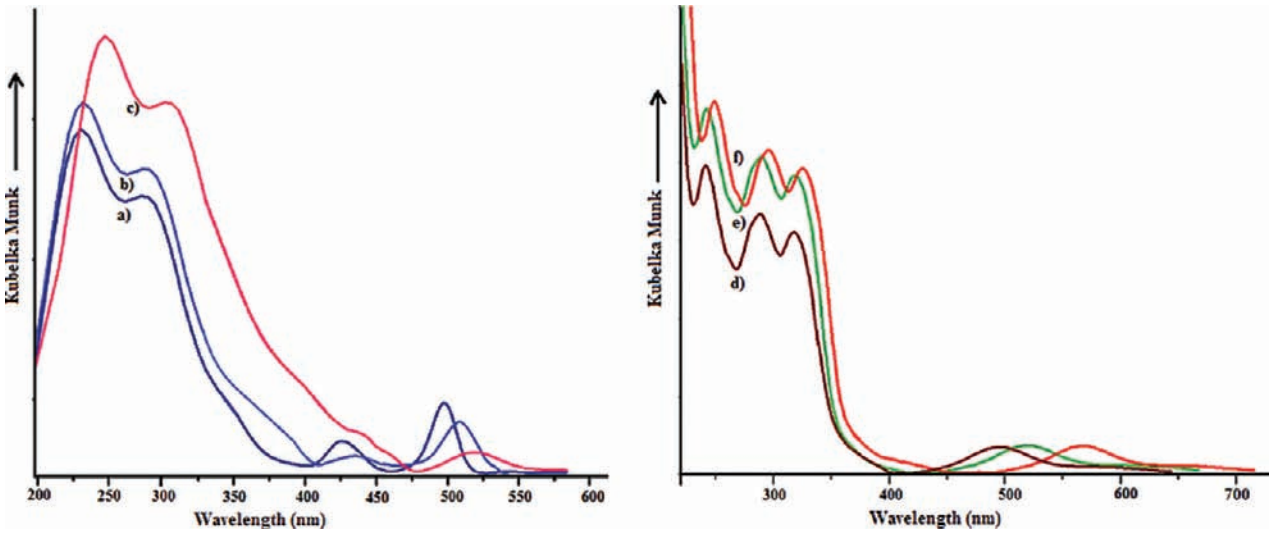

Figure 6. UV−vis/DRS spectra of (a) Fe-Salen-LiY, (b) Fe-Salen-NaY, (c) Fe-Salen-KY, (d) Fe-Salophen-LiY, (e) Fe-Salophen-NaY, and (f) Fe-Salophen-KY showing the red shift of the charge transfer bands with the progressive increase in size of the counterions.

cation gives rise to changes in donor strength (basicity), i.e., the increase in negative charge density of the framework oxygen leading to the progressive red shift of the lower and higher energy bands.

The presence of the similar electronic transitions in the encapsulated complexes in comparison to the neat complex in solution gives evidence for the formation of complexes inside the supercage of zeolite-Y. However, the shifting of peaks on encapsulation of the complexes into various cation-exchanged zeolites implies that the electronic transitions are greatly influenced due to the interaction of the metal complexes with the walls of zeolite framework.

3.1.5. Relationship of the Lower Energy and Higher Energy Band with the Framework Donor Strength. Since the increase in the electropositivity of the countercation gives rise to the increase in the donor strength (basicity) of the framework, we examined the relationship between the spectral shift and the framework donor strength. For this purpose, in fact, it is necessary to get the ionization potentials of zeolite frameworks, $I_p(Z)$, as the direct measures of the framework donor strengths as in the case of small molecules. However, the corresponding values of $I_p(Z)$ are not available at this stage for zeolites Y; therefore, we used Sanderson's partial charges of the framework oxygen atoms. Sanderson's partial charges of the framework oxygen atoms for the zeolites are calculated on the basis of their chemical compositions listed in Table 4.

It can be seen from Figure 7 that for both the iron complexes encapsulated in various alkali exchange zeolites a red shift of the lower and the higher energy band indeed arises in response to the increase in the negative charge density of the framework oxygen, i.e., upon increasing the framework donor strength. The observed sharp increase in the LMCT bands upon increasing the size of the alkali cation indicates that the degree of red shift of the CT band is sensitive toward the donor strength of zeolite-Y.

3.1.6. EPR Spectroscopy. Powder EPR spectra of neat Fe-Schiff-base complexes and the encapsulated complexes were obtained with microwaves in the 9442−10 000 MHz region at 77 K with fields corresponding to about 50−500 mT. Figure 8 shows the EPR spectra of neat complexes and the encapsulated complexes in various alkali exchanged zeolite-Y, and the *g*-values

Table 4. Type of Zeolites, Sanderson's Electronegativity, and Sanderson's Partial Negative Charge Density on the Framework Oxygen $(-\delta_o)^a$

zeolite	Sanderson's electronegativity	$-\delta_o$
Li^+-Y	2.67	0.24
Na^+-Y	2.60	0.26
K^+-Y	2.58	0.27

[a]The Sanderson's electronegativity of each M^+-exchanged zeolite S_z was calculated according to the equation $S_z = (S_M{}^p S_H{}^q S_{Al}{}^r S_{Si}{}^t S_o{}^u)^{1/(p+q+r+t+u)}$, where S_M, S_H, S_{Al}, S_{Si}, and S_O represent the Sanderson's electronegativities of the alkali metal, hydrogen, aluminum, silicon, and oxygen, respectively, and *p*, *q*, *r*, *t*, *u* represent the number of the corresponding element in a unit cell, respectively. The Sanderson's partial charge of the framework oxygen (δ_o) was calculated using the equation $\delta_o = (S_z - S_o)/(2.08 S_o{}^{1/2})$. The values are taken from: Huheey, J. E.; Keiter, E. A.; Keiter, R. L. *Inorganic Chemistry*, 4th ed.; Harper Collins College Publications: New York, 1993.

for all the neat and encapsulated complexes are given in Table 5. As expected, for axially distorted octahedral Fe^{3+} ions, the broad single line having $g_\parallel$ value >4.23 in all the cases corresponds to the low spin d^5 ion in the weak field region. Many monomeric iron(III) complexes show a signal of this nature.[42,43] In the case of the neat complex, the signals having $g_\parallel = 2.03$ and $g_\perp$ value of 1.980 could probably arise from the location of unpaired electrons in the organic ligands of the complex or due to the presence of impurity radicals. The hyperfine lines are not resolved in neat Fe-Salen complex even at 77 K. A similar broad signal at $g \approx 4.2$ prevails in the encapsulated complexes indicating the presence of low-spin iron(III) configurations in them. In the case of encapsulated Fe-Schiff-base complexes, the hyperfine splitting is resolved, and the number of hyperfine lines is greater in the case of the Shiff-base complexes encapsulated in Li^+ ion exchanged zeolites. The anisotropy in the *g*-values suggests that the Fe-complexes get rhombically distorted under the influence of zeolite matrix. It can be seen from Table 5 that the $g_\parallel$ values increase with the increase in the size of the alkali exchanged cations and $g_\perp$ values gradually decrease. The difference in the *g*-values between the neat and the encapsulated

dx.doi.org/10.1021/ic201959g | *Inorg. Chem.* 2012, 51, 1657−1674

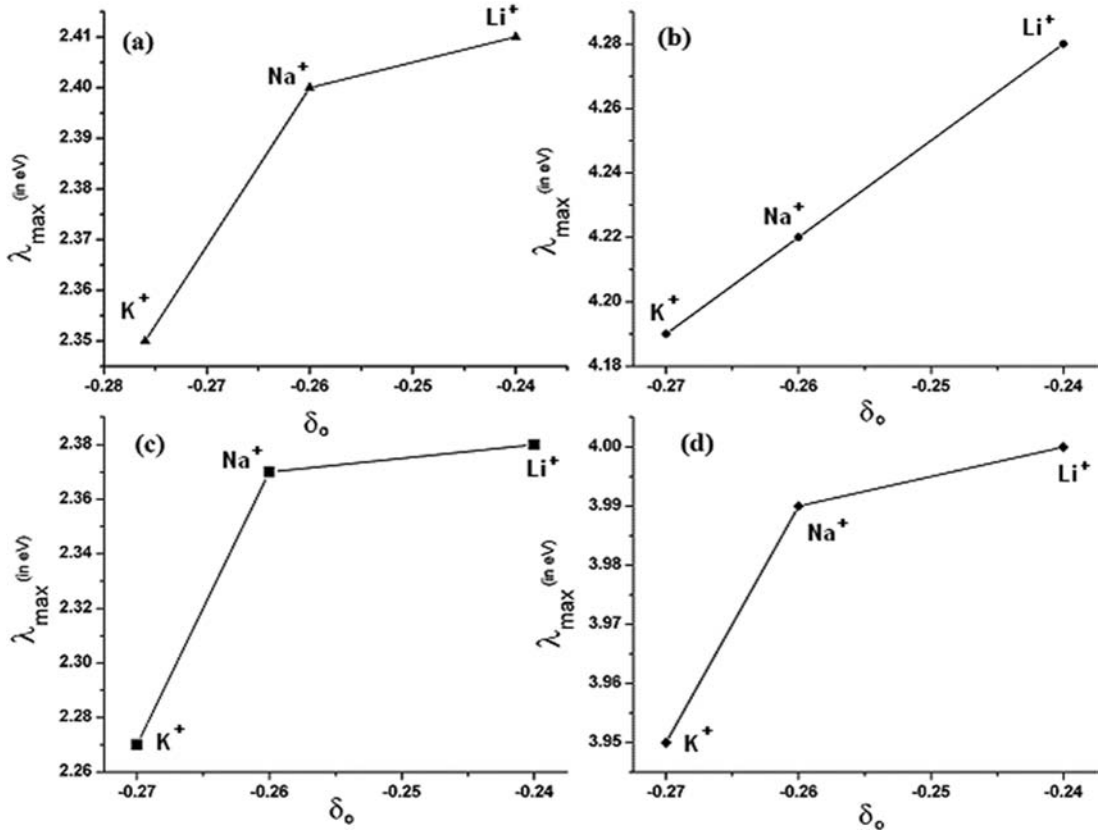

Figure 7. Relationship between the (a) lower energy bands of encapsulated Fe-Salen, (b) higher energy bands of encapsulated Fe-Salen, (c) lower energy bands of encapsulated Fe-Salophen, and (d) higher energy bands of encapsulated Fe-Salophen in various alkali metals exchanged in zeolite with the calculated Sanderson's partial charge of the framework oxygen of $M^{+}Y$.

complexes gives a clear indication for formation of Fe-complexes inside zeolite.

3.1.7. Cyclic Voltammetry. Cyclic voltammetry provides information on the nature of intrazeolite complexes that may not be readily apparent from spectroscopic studies. Zeolites are basically insulators, so the encapsulation of transition metal complexes makes these molecular sieves to show redox behavior if they are encapsulated inside the cavities or bound to the surfaces within zeolite lattice. Shaw and co-workers[44] first proposed two possible mechanisms: intrazeolite and extrazeolite mechanism for electron transfer associated with encapsulated transition metal complexes within the supercage of zeolite and surface bound metal complexes, respectively, based on zeolite modified electrodes (ZMEs). Although these mechanistic assignments are controversial, there are various reports demonstrating the redox behavior of transition metal complexes encapsulated in zeolite cavities.[45−47]

Bedioui et al.[48−52] have synthesized metal Schiff-base complexes inside the supercages of zeolites (ship-in-a-bottle). They have concluded that the electroactive species are reduced or oxidized within the supercages of zeolite-Y (intrazeolite electron transfer). Shaw and co-workers[53,54] and others have studied the electron transfer mechanism of methyl viologen (MV^{2+}) exchanged zeolite-Y. Rolison[55] and Baker et al.[56] showed that the electron transfer takes place at the zeolite−solution interface (extrazeolite electron transfer). Calzaferri et al.[57] studied the potential for strong acidity. Very recently, Zhang et al. studied the electrochemical behavior of M (Co, Fe, Mn) (Salen) complexes as a component of modified glassy carbon electrode.[26]

So, relying on the ZMEs to obtain information for zeolite encapsulated transition metal complexes we have studied the redox activity of the Fe (III) Schiff-base complexes and the effect of counterions on the redox behavior of these complexes. Initially, we studied the electrochemical behavior of the synthesized neat iron complexes using 0.1 M TBAP as supporting electrolyte in DCM solution and then compared these with the encapsulated complexes using modified glassy carbon electrode.

a. Electrochemistry of the Neat Fe(III) Schiff Base (Salen, Salophen) Complexes. Typical cyclic voltammograms of Fe(III)-Salen and -Salophen are shown in Figure 9a,b, respectively. The Fe(III)-Salen complex shows a quasireversible peak with a cathodic reduction peak at −0.461 V corresponding to the one-electron reduction process represented as $[Fe^{III}(L)_2X]^{2+} + e^{-} \rightarrow [Fe^{II}(L)_2]^{2+} + X^{-}$. The reduction of the Fe(III) complex results in the loss of its axial ligands, since the electron is added to the antibonding d_{z^2}-orbital. Upon reversal of the scan direction, the Fe(II) complex is reoxidized at −0.411 V. In case of the Fe(III)-Salophen, the cathodic reduction peak occurs at −0.526 V and the corresponding anodic oxidation at −0.335 V. This shows that the redox behavior of this complex is quasi-reversible. In addition to the redox couple both the Fe-Salen and Fe-Salophen complexes show an additional cathodic peak at 0.847 and 0.898 V, respectively. The difference in the electrochemical behavior of the two complexes indicates the effect of ligand substitution on the redox potential of complexes.

b. Electrochemistry of the Encapsulated Fe(III) Schiff Base (Salen, Salophen) Complexes in Various Zeolites. The cyclic voltammograms of the encapsulated complexes in various cation exchanged zeolites are shown in Figure 9c−e,g−i, and E° values

dx.doi.org/10.1021/ic201959g | Inorg. Chem. 2012, 51, 1657−1674

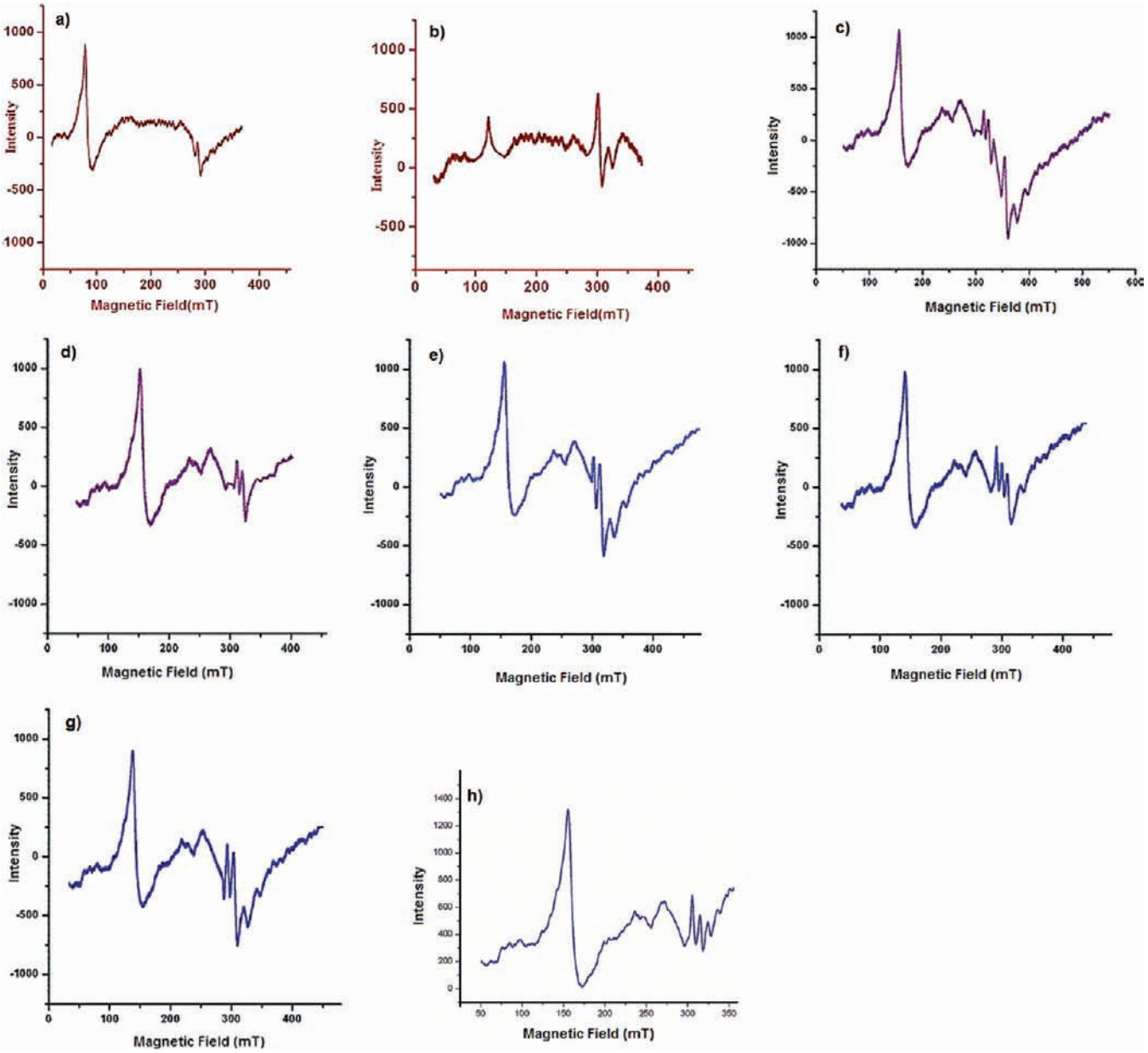

Figure 8. Powder EPR spectra of (a) neat Fe-Salen complex, (b) neat Fe-Salophen complex, (c) Fe-Salen-LiY, (d) Fe-Salen-NaY, (e) Fe-Salen-KY, (f) Fe-Salophen-LiY, (g) Fe-Salophen-NaY, (h) Fe-Salophen-KY, at 77 K.

Table 5. EPR Analysis of the Neat and the Encapsulated Iron Complexes

sample	$g_{\parallel}$	$g_{\perp}$	$g_{\parallel}$
Fe-Salen	4.24	2.03	1.986
Fe-Salophen	4.24	2.02	1.978
Fe-Salen-Li Y	4.22	2.147	2.110
Fe-Salen-Na Y	4.21	2.120	2.140
Fe-Salen-KY	4.20	2.107	2.180
Fe-Salophen-Li Y	4.23	2.148	2.122
Fe-Salophen-Na Y	4.22	2.132	2.150
Fe-Salophen-KY	4.20	2.09	2.22

are given in Table 6. Several interesting changes are found in the redox behavior of the encapsulated complexes: (i) the redox signals are broad and persist for an interval of 30−60 min, and (ii) the peak potentials are shifted as compared to those of the neat complexes as can be seen from Table 6. In the case of the Fe-SalenY complex encapsulated in various zeolites, this shows reversible peaks and an additional irreversible cathodic peak. The reversible peaks are associated with the one electron $Fe^{III} \rightleftharpoons Fe^{II}$. The additional cathodic peak may be due to the partially associated Fe^{III}(Salen) species. Bedioui et al.[44] also reported several additional peaks in the cyclic volltammetry of {Co(Salen)}NaY ZME in DMSO or CH_3CN when compared to homogeneous counterparts. It can be seen from Table 6 and Figure 9 that significant differences in the cyclic voltammograms (peak potential, peak shapes, and relative integrated current areas) occur as the size of alkali cation changes from Li^+ to K^+. A gradual increase in size of the alkali cations shifted the reduction potential to more negative values. One possible reason is that during the exchange process some of the alkali metal cations diffuse into the cavities and can reside in the

dx.doi.org/10.1021/ic201959g | Inorg. Chem. 2012, 51, 1657−1674

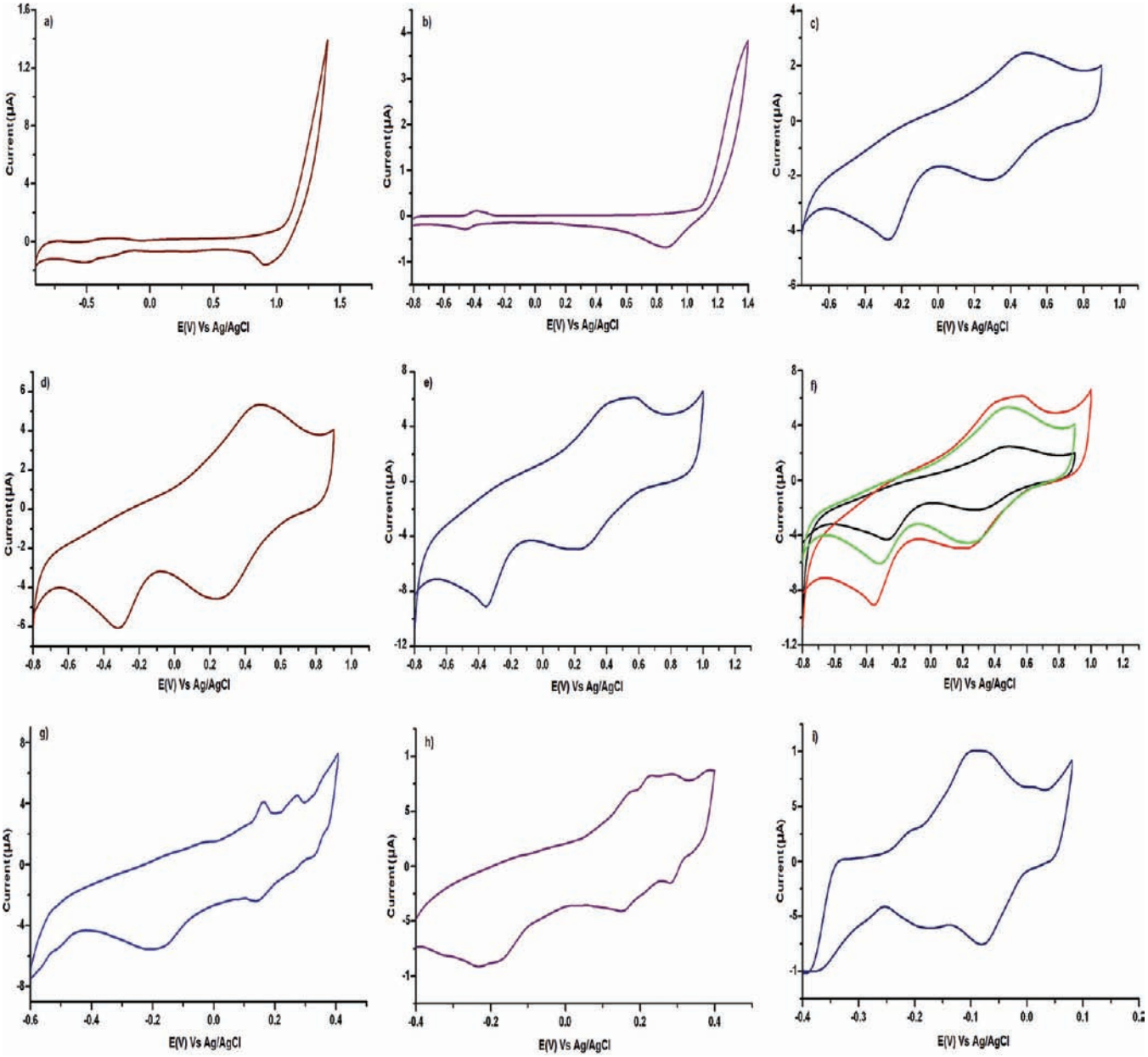

Figure 9. Cyclic voltammograms of (a) neat Fe-Salen, (b) neat Fe-Salophen complexes taken in DCM using 0.1 M TBAP as supporting electrolyte, (c) Fe-Salen-LiY, (d) Fe-Salen-NaY, (e) Fe-Salen-KY, (f) overlay of c−e, (g) Fe-Salophen-LiY, (h) Fe-Salophen-NaY, (i) Fe-Salophen-KY, taken as a component of ZME in DCM using 0.1 M TBAP as supporting electrolyte.

Table 6. Oxidation and Reduction Peak Potential Values (in V) for Neat and Encapsulated Fe-Schiff-Base Complexes

sample	E^1_{oxd}	E^2_{oxd}	E^1_{red}	E^2_{red}	E^{av}_{oxd}	E^{av}_{red}
Fe-Salen	−0.411		−0.461	0.847		0.193
Fe-Salophen	−0.335		−0.526	0.898		0.186
Fe-Salen-Li Y	0.471		0.301	−0.273		0.014
Fe-Salen-Na Y	0.465		0.237	−0.312		−0.037
Fe-Salen-KY	0.567		0.217	−0.352		−0.067
Fe-Salophen-Li Y	0.162	0.274	0.323	0.141	0.218	0.232
Fe-Salophen-Na Y	0.225	0.283	0.235	0.156	0.254	0.195
Fe-Salophen-K Y	−0.206	−0.087	−0.080	−0.176	−0.147	−0.128

channels that exist in the lattice of zeolites and influence the intrazeolite electron transport.

In the case of the iron(III)-Salophen complex encapsulated in various zeolites two quasireversible peaks are obtained. The first cathodic wave is due to the reduction of Fe(III) to Fe(II), and the second cathodic peak is due to the reduction of Fe(II) to Fe(I). Upon reversal of the scan, it shows the corresponding oxidation peaks, i.e., from Fe(I) to Fe(II) and Fe(II) to Fe(III).

dx.doi.org/10.1021/ic201959g | Inorg. Chem. 2012, 51, 1657−1674

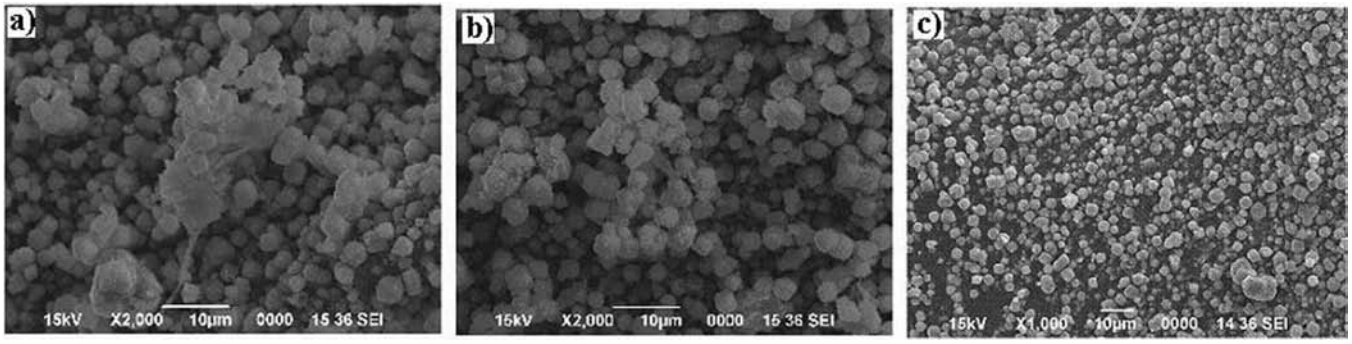

Figure 10. Typical SE micrographs of (a) encapsulated Fe-Salen complex, (b) encapsulated Fe-Salophen complex before Soxhlet extraction, and (c) encapsulated complexes after Soxhlet extraction.

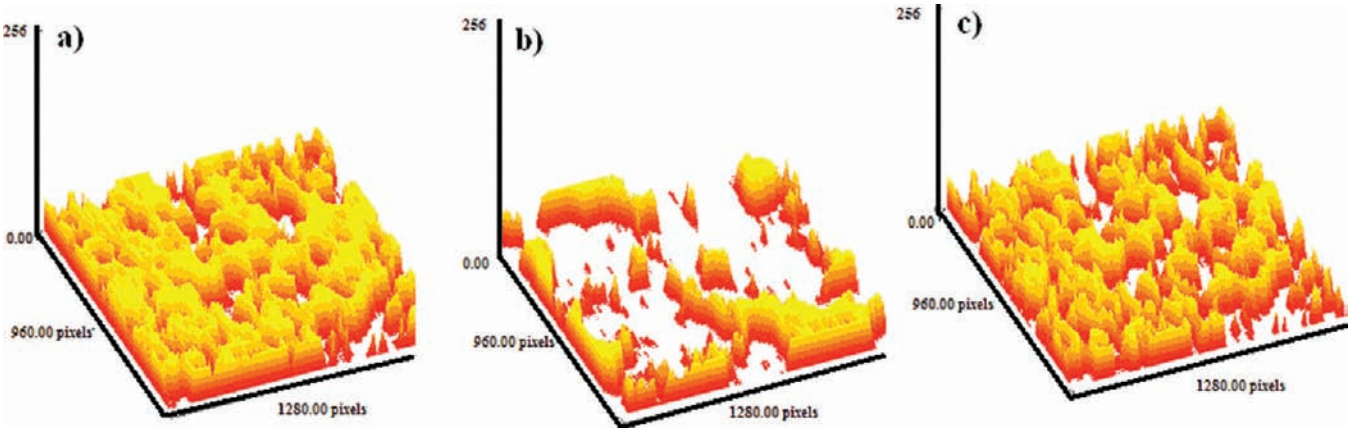

Figure 11. Surface plot of (a) pure NaY, (b) encapsulated Fe complexes before Soxhlet extraction, and (c) encapsulated Fe complexes after Soxhlet extraction. The white portion represents the presence of an extraneous substance on surface of zeolite Y.

The peaks become broadened and yielded a well-defined cyclic voltammogram of the encapsulated complexes as the size of the cation increases. Most importantly the average E^{av}_{red} values are shifted to more negative values in both the encapsulated complexes as the countercation size increases. The alternation of the redox potential and the shifting of the peak potential toward more negative values as the size of the cation increases indicate that the iron becomes stabilized in its Fe^{3+} state when encapsulated into the zeolites; i.e., zeolite-Y exchanged with large alkali metal cation favors the oxidation of Fe(I) to Fe(II) and Fe(II) to Fe(III).

The alternation in the redox potentials of iron Schiff-base complexes encapsulated in various zeolites suggests that the complex suffers from a space constraint imposed by the zeolite matrix leading to geometrical distortion, thereby changing the crystal field stabilization energy and the peak potentials in comparison to the neat complexes.

3.1.8. Scanning Electron Microscopy (SEM) Analysis. Encapsulation of Fe(III) complexes of Salen and Salophen ligands in Y zeolite is accomplished using a flexible ligand synthesis scheme. The ligands, which are flexible enough to diffuse through the zeolite channels, react with the pre-exchanged metal ions in the supercage to afford the encapsulated complexes. The product material is purified by extensive Soxhlet extraction with suitable solvents to remove unreacted ligand and surface complexes. The samples did not change their color on purification, indicating that the complexation has occurred in the cavities. SE micrographs of Fe-Salen-Y and Fe-Salophen-Y taken before Soxhlet extraction and that of Fe-Salophen-Y taken after Soxhlet extraction are shown in Figure 10a–c, respectively, as a representative case. In the SEM taken before purification, the complexes deposited on the external surface are visible. In the SEM of finished products, no surface complexes are seen, and the particle boundaries on the external surface of zeolite are clearly distinguishable. This is much clearer from the surface plot shown in Figure 11a–c, where the white portion in Figure 11b indicates the surface occupied by extraneous complexes or the uncomplexed ligands. The surface plot of the SE-micrograph taken after Soxhlet extraction showed no such white portion indicating the efficiency of the purification procedure to effect complete removal of extraneous complexes, leading to well-defined encapsulation in the cavity. Moreover, no crystalline patterns are seen for the encapsulated complexes: this might be due to their fine distribution in the lattice.

3.1.9. Thermal Analysis. The TG patterns of parent NaY, iron exchanged zeolite (FeY), neat Fe-Schiff complexes, and encapsulated Fe Schiff-base complexes (Salen and Salophen) are displayed in Figure 12. The comparison of thermogravimetric analyses for Fe-Schiff-base complexes and encapsulated Fe-Schiff-base shows that the neat Fe-Salen complex has three weight loss steps at about 96, 322, and 448 °C while the Fe-Salophen complex shows four weight loss steps at about 116, 200, 402, and 500 °C. On the basis of the weight changes, the first weight-loss step in both neat complexes corresponds to the loss of a water molecule as an endothermic phenomenon. The second weight loss at 200 °C in the case of the Fe-Salophen complex may be related to the loss of Cl_2. There is a sharp

dx.doi.org/10.1021/ic201959g | *Inorg. Chem.* 2012, 51, 1657–1674

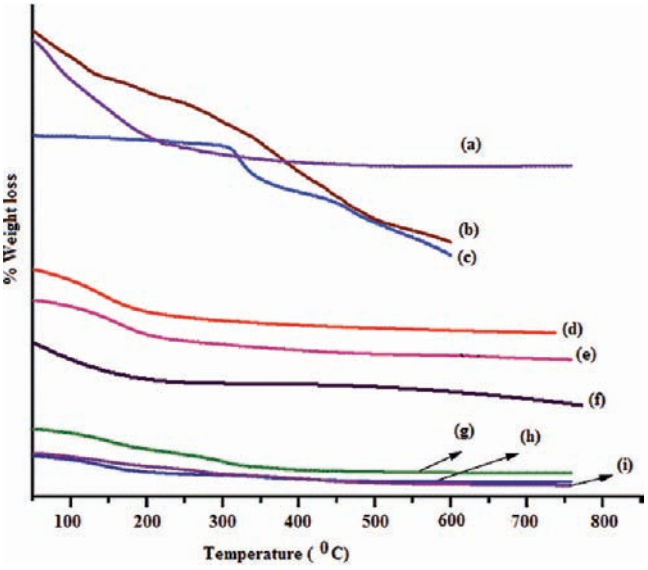

Figure 12. Thermogravimetric analysis (TGA) patterns of (a) NaY, (b) neat Fe-Salophen complexes, (c) neat Fe-Salen, (d) Fe-Salophen-LiY, (e) Fe-Salophen-NaY, (f) Fe-Salophen-KY, (g) Fe-Salen-LiY, (h) Fe-Salen-NaY, (i) Fe-Salen-KY.

weight change at 322 °C and at 402 °C in the case of Fe-Salen and Fe-Salophen which is attributed to the loss of Salen and Salophen groups, respectively. There is a weak peak at 448 °C and at 500 °C in the case of both of the complexes, which may be due to sublimation of part of Fe_2O_3. However, for the corresponding encapsulated complex the weight loss extended up to 560 °C, which indicates that the thermal stability is greatly enhanced and there is no peak at 100−120 °C indicating the absence of water of crystallization. This gives another piece of evidence for the inclusion of Fe-Schiff-base complexes in Na−Y. On the basis of thermal analysis data, we may conclude that zeolite encapsulated Fe-Salen may be treated thermally without any significant decomposition.

3.1.10. Theoretical Calculation. The selected bond lengths and bond angles obtained from VWN/DN level calculations for the neat and the encapsulated complexes are presented in Table 7. The geometrical parameters are relatively in good agreement with the reported experimental values.[58,59] However, the geometrical parameters for the encapsulated complexes show slight deviations from those of the neat complexes. The change in the bond length and bond angle on encapsulation may be attributed to the influence of the zeolite framework. The valence electrons in zeolites are distributed all over the framework atoms as a partially delocalized electron cloud. At a relatively short distance between the complex and the walls of the zeolite cavities, the electron−electron repulsion will be operative, which will influence the structural and electronic properties of the encapsulated complexes.

For all the considered complexes, the patterns of the occupied and the unoccupied orbitals are qualitatively similar. The energies of the HOMO and LUMO for the neat iron(III)-Schiff-base complexes and those encapsulated in zolite-NaY are represented as a comparative energy profile diagram in Figure 13. It can be seen from Figure 13 that the energies of both the HOMO (−12.65 eV) and the LUMO (−12.22 eV) for the neat $[Fe(Salophen)_2]^{3+}$ complex lie higher in energy in comparison to those of the $[Fe(Salen)_2]^{3+}$ (E_{HOMO} = −12.97 eV and E_{LUMO} = −12.489 eV). Upon encapsulation, the HOMO and LUMO levels

Table 7. Selected Bond Lengths (in Å) and Bond Angles (in deg) of the Optimized Neat and Encapsulated Fe-Schiff-Base Complexes

	$[Fe\text{-}SalenCl]^{2+}$	Fe-SalenY	$[Fe\text{-}SalophenCl]^{2+}$	Fe-SalophenY
		Bond Lengths		
Fe−O1	1.79	1.776	1.80	1.840
Fe−O2	1.81	1.839	1.79	1.858
Fe−N1	1.89	1.920	1.87	1.950
Fe−N2	1.84	1.830	1.89	1.970
Fe−Cl	2.09		2.11	
		Bond Angles		
O1−Fe−O2	87.51	83.45	86.13	75.53
O1−Fe−N1	88.77	89.28	92.51	86.44
O1−Fe−N2	124.45	119.57	165.97	120.77
O2−Fe−N1	173.41	169.74	157.42	145.43
O2−Fe−N2	92.73	94.27	91.38	86.54
N1−Fe−N2	84.88	82.98	84.48	77.62
O1−Fe−Cl	130.54		101.26	
O2−Fe−Cl	95.65		105.41	
N1−Fe−Cl	90.89		96.95	
N2−Fe−Cl	104.72		92.69	

get destabilized and the increasing order of energies (for both HOMO and LUMO levels) is Fe-Salophen-NaY > Fe-Salen-NaY > Fe-Salophen > Fe-Salen. This change in the energies of the frontier orbital can be further correlated to the reducing ability of Fe(III) or to the oxidation of Fe(III) to Fe(IV) by molecular oxygen which is reported to be the rate-determining step in oxidative coupling reaction of 2-napthol to BINOL using molecular oxygen (discussed below). Since the HOMO of the Fe-Salophen complexes comparatively lies higher in energy than Fe-Salen, it will have a higher tendency to get oxidized. In contrast, since upon encapsulation the HOMO is more higher-lying in both the systems in comparison to the neat complexes, they will have a higher tendency to get oxidized and enhance the rate of the reaction. Also, the reactivity of Fe-Salophen-NaY will be more in comparison to the Fe-Salen-NaY system, and this result is in accordance with our experimental results. Further, from Table 8 it can be seen that the global hardness of Fe-Salophen-NaY is less in comparison to its solution analogue and other complexes and has higher value of global softness (S). According to the maximum hardness principle[60,61] and the minimum polarizability principle (MPP),[62] the hardness measures the stability and softness (polarizability) measures the reactivity. Thus, it can be said that among the four systems the Fe-Salophen complex encapsulated in NaY will show higher reactivity with minimum hardness and maximum softness.

The Hirshfeld population analysis (HPA) of the Fukui functions (f_k^+ and f_k^-) calculated at the same level of theory for the metal atom and those coordinated to it are given in Table 9. It can be seen that the values of the Fukui functions at the metal center decrease in the order Fe-Salen > Fe-Salophen > Fe-SalenY > Fe-SalophenY. Some of the reported calculations have shown that a minimum Fukui function and maximum net charge site are preferred for a hard−hard interaction whereas a soft−soft interaction is preferred at the site with maximum Fukui function.[63−65] Among our four systems, the central iron atom in the Fe-SalophenY complex possesses maximum positive Mulliken and Hirshfeld charges calculated at VWN/DN level of theory and minimum value of the Fukui function.

dx.doi.org/10.1021/ic201959g | Inorg. Chem. 2012, 51, 1657−1674

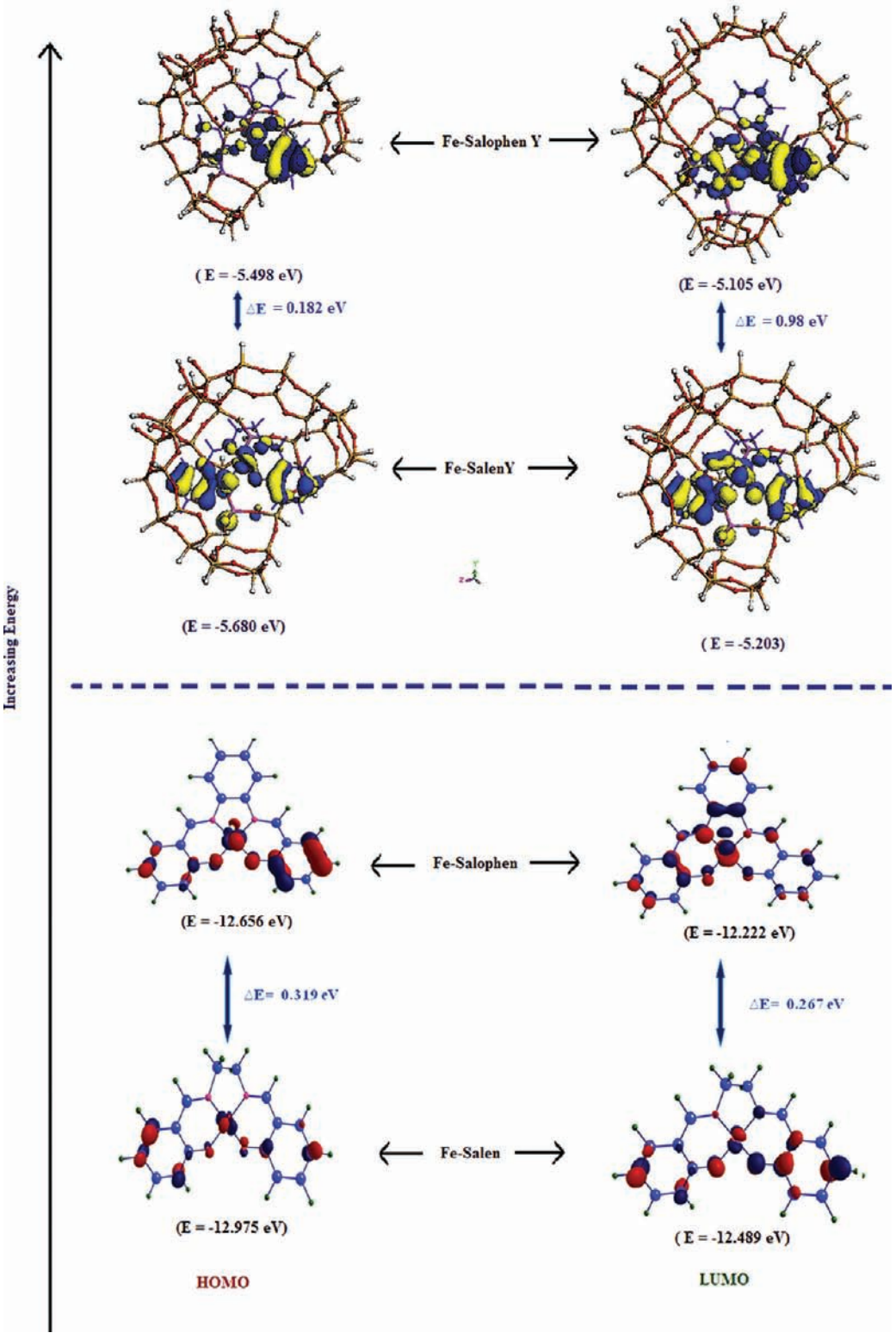

Figure 13. Schematic representation of the HOMO and LUMO level of the neat and the encapsulated Fe-Schiff-base complexes. Orbitals below the dotted line represent the positions of the HOMO (left-hand side) and LUMO (right-hand side) of the neat complexes in increasing order of energy, and those above the dotted line represent the energies of the frontier orbitals of the corresponding encapsulated complexes.

The order of positive Mulliken and Hirshfeld charges at the central atom are Fe-SalophenY (0.92) > Fe-SalenY (0.85) > Fe-Salophen (0.55) > Fe-Salen (0.53) and Fe-SalophenY (0.25) > Fe-SalenY(0.24) > Fe-Salen (0.20) > Fe-Salophen (0.19), respectively. Thus, it indicates that the central iron atom in Fe-SalophenY complex with maximum positive charge and minimum value of Fukui function is the most preferential site for interacting with hard species. This enhancement of hard−hard interaction on encapsulation into the zeolite framework also reflects the higher catalytic activity. The catalytic conversion of

dx.doi.org/10.1021/ic201959g | *Inorg. Chem.* 2012, 51, 1657−1674

Table 8. Calculated Energies of HOMO and LUMO Levels (in eV), Global Hardness (η, in eV), and Softness (S, in eV)

complex	E_{LUMO}	E_{HOMO}	η	S
Fe-Salen	−12.489	−12.975	0.243	2.057613
Fe-SalenY	−5.203	−5.680	0.238	2.096436
Fe-Salophen	−12.222	−12.656	0.217	2.304147
Fe-SalophenY	−5.105	−5.498	0.196	2.544529

2-napthol to BINOL proceeds via the coordination of naptholate ion at the vacant site of Fe(III)-Schiff-base complex, and it involves a hard−hard interaction. Therefore, the first step, i.e., the interaction of naptholate ion with the central metal atom to form a pentacordinated iron complex, is much more preferred in Fe-SalophenY.

4. CATALYTIC ACTIVITY

4.1. Oxidative Coupling of 2-Napthol by Neat and Zeolite Encapsulated Fe-Schiff-Base Complexes. The oxidative coupling of 2-napthol is a representative reaction mode for direct synthesis of 1,1′-binapthol (BINOL) whose optically pure derivatives are regarded as versatile chiral auxiliaries and ligands in asymmetric synthesis. However, these substances remain largely unstudied because of their difficulties in synthesis. Most of the recently published highly enantioselective syntheses of BINOL and its derivatives are based on naphthol coupling catalyzed by chiral complexes containing one or two metal center(s), viz., vanadium, iron, or copper.[27,28,66−69] The formation of a self-dimerized chiral assembly of vanadium complexes on a SiO_2 surface is also reported to promote the enantioselective naphthol coupling.[64] Also, the search continues for a new heterogeneous catalyst capable of carrying out the selective oxidative coupling of 2-napthol.

We found that the encapsulated achiral iron-Schiff-base complex within zeolite-Y cages creates a catalyst that allows highly selective transformation of β-naphthol to BINOL under aerobic condition without any additive. The catalytic activities of the encapsulated Fe-complexes and their homogeneous analogues in the oxidative coupling of 2-napthol are shown in Table 10. The catalytic activities of the complexes are tested in different solvents like dichlromethane (DCM), dimethylformamide (DMF), and toluene refluxing at 30 °C. Most of the complexes showed very poor or no catalytic activity in these solvents at 30 °C. However, on increasing the temperature up to 60 °C in toluene, the neat complexes give the racemic mixture with moderate yield. The Fe-Salophen complex shows high selectivity and gives better yield compared to the Fe-Salen complex. Under the same conditions, the catalytic activities of the encapsulated complexes are tested for oxidative coupling of 2-napthol. It can be seen from the data given in Table 10 that the encapsulated Fe-Schiff-base complexes give high percentage yield and selectivity in comparison with the neat complexes. Increasing the amount of catalyst decreased the yield of the desired product with more byproduct. Therefore, the reaction is performed with 10 mg of the catalysts. Among all the complexes, Fe-Salophen-KY shows good conversion of 2-napthol to BINOL. Blank experiments carried out without the catalyst under identical experimental conditions do not produce BINOL, indicating the participation of the iron complex in the reaction path. The use of a stoichiometric amount of complexes as oxidizing agent under nitrogen atmosphere does not yield the product, indicating that oxygen is essential for the reaction. The time required for this catalytic conversion is found to be less in the case of the encapsulated complexes in comparison to the corresponding neat complexes. The desired product is isolated by column chromatography, enatioselectivities are obtained by HPLC analysis on a chiral stationary phase column (Daisel Chiralcel AS-H), and the optical purities are determined by chiroptical comparison with the literature value. The iron-exchanged zeolites do not show any catalytic activity up to 6 days so herein we do not account for the productivity which results in the presence of such catalyst.

Table 9. Hirshfeld Population Analysis of Fukui Functions for the Neat and Encapsulated Complexes

	$[Fe\text{-}Salen]^{3+}$		$[Fe\text{-}Salophen]^{3+}$		Fe-Salen-NaY		Fe-Salophen-NaY	
selected atoms	f_k^+	f_k^-	f_k^+	f_k^-	f_k^+	f_k^-	f_k^+	f_k^-
O_1	0.032	0.031	0.026	0.025	0.011	0.010	0.018	0.017
O_2	0.030	0.029	0.024	0.024	0.016	0.016	0.012	0.012
Fe	0.032	0.031	0.020	0.019	0.012	0.012	0.008	0.007
N_1	0.013	0.013	0.010	0.010	0.008	0.008	0.010	0.009
N_2	0.014	0.014	0.012	0.012	0.007	0.007	0.007	0.007

Table 10. Oxidative Coupling of 2-Naphthol in Toluene at 60 °C with Reactions Carried Out in Toluene with Catalyst (10 mg) on a 5 mmol Scale under Aerobic Conditions.

catalyst	time	(%) yield[a]	yield in mmol	Fe-atom in catalyst[b] (mmol)	(%) conversion[c]	R:S (%)[d]	TON
NaY	72 h	nil	nil		nil		
Fe-Salen	72 h	12	0.6	0.023	50	50:50	26
Fe-Salophen	66 h	18	0.9	0.023	56	50:50	39
Fe-Salen-LiY	28 h	20.2	1.01	0.0097	70	50:50	104
Fe-Salen-NaY	24 h	26.5	1.32	0.0098	84	54:46	135
Fe-Salen-KY	21 h	30.2	1.51	0.0098	89	62:38	154
Fe-Salophen-LiY	22 h	35.5	1.77	0.0098	86	52:48	181
Fe-Salophen-NaY	20 h	38.3	1.91	0.0096	92	56:44	199
Fe-Salophen-KY	17 h	45.2	2.26	0.0097	97	70:30	232

[a]Determined by chromatographic separation. [b]Amount of Fe-atom in mmol present per 10 mg of catalyst. [c]Conversion refers to fraction of starting material consumed in the reaction. [d]Determined by chiroptical comparison with the literature value and HPLC analysis on a chiral stationary phase column (Daisel Chiralcel AS-H).

dx.doi.org/10.1021/ic201959g | Inorg. Chem. 2012, 51, 1657−1674

Oxidative coupling of 2-napthol with the neat complexes resulted in the formation of racemic BINOL only. Further, we could isolate only 12% of the desired product in the case of the reaction catalyzed by the Fe-salen complex. This may be due to chelate formation which remains bound with the catalyst (Fe-Salen) until the coupling reaction is completed. However, oxidative coupling of 2-napthol with Fe-Salophen and Fe-Salen complex encapsulated in potassium exchanged zeolite under similar conditions results in 40% and 24% ee. This enhancement of selectivity toward the *R*-conformation on encapsulation of the complexes into various alkali exchanged zeolite may be due to the combined action of spatial confinement and metal-ion coordination of the substrate within the zeolite supercage both of which greatly reduce the freedom of the substrate and entropically manipulate the stereochemical outcome. It may be noted herein that, during catalytic conversion of 2-napthol to BINOL, some mass losses have occurred. The high mass loss may be due to strong adsorption of the product, i.e., BINOL, on the metal complex and on the surface of the zeolite catalyst either through complexation with potential surface atoms like iron, since BINOL has a very strong affinity of chelate formation, or through entrapment into the pores of the catalysts. The complexation of the substrate (naphthol) with the surface catalyst metal atoms also cannot be ruled out. Some unidentifiable products could also have been formed and held on the surface. This along with chelate formation[27,70,71] accounts for the mass imbalance that occurs during catalytic conversion of 2-napthol to BINOL.

The turnover number (TON) increases on encapsulation of the iron-Schiff-base complexes into different cation exchanged zeolites. It can be seen from Figure 14 that the TON increases

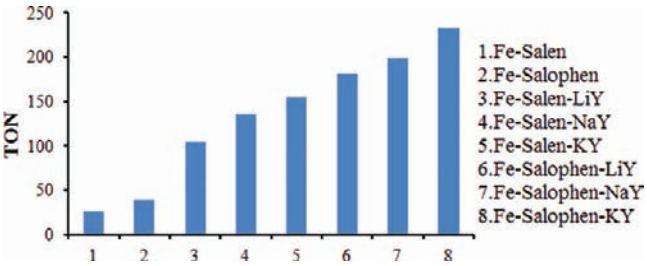

Figure 14. TON for the catalytic oxidative coupling of 2-napthol using various iron(III) Schiff-base complexes.

as the size of the alkali cation increases and has been found to be maximum in the case of the coupling reaction catalyzed by Fe-Salophen-KY (232), which is almost 6 and 9 times higher than the neat Fe-Salen and Fe-Salophen complexes, respectively (Table 10). This increase in the TON further reflects that the zeolite matrix provides an environment for achieving particular reactions by varying the exchangeable alkali metal cations.

Among the homogeneous catalysts, the complex bearing the phenyl group shows the higher catalytic activity. This is in accordance with our cyclic voltametric study and theoretical study where we found that the second half-wave reduction potential of the Fe-Salophen complex to be more negative and with a higher lying HOMO than the Fe-Salen. In contrast to the neat complexes the catalytic conversion of the encapsulated complexes is found to be greater, and interestingly, the activity increases with increase in size of the counterion, as can be seen from the data in Table 10. This tendency is corroborated with shifting of the E^{av}_{red} reduction potential toward more negative values. Also, it has been observed from voltammogram of the encapsulated complexes in various alkali exchanged zeolites that, as the size of cation increases, electron flow is perturbed and influences the peak potential which in turn affects the catalytic activity of the encapsulated complexes. The values of the average reduction potential of the neat and the encapsulated complexes indicate that in the case of the neat complexes the reduction potential is close to that of the molecular oxygen so the reduction of molecular oxygen and consequently the oxidation of Fe(III) to Fe(IV) which is considered to the rate determining step in oxidative coupling reaction of 2-napthol in the presence Fe-Salen complex as catalyst is slow. However, in the case of the encapsulated complexes the reduction potential lies below the reduction potential of molecular oxygen, and it becomes more negative as the size of the alkali metal cation becomes more electropositive. Hence, the reduction of molecular oxygen in the presence of the Fe-Schiff-base complex encapsulated in K^+ ion exchanged zeolite-Y becomes faster and shows better catalytic conversion in comparison to the neat complexes and its counterparts. So, it can be said that the catalytic activity of the iron-Schiff-base complexes toward the oxidative coupling of 2-napthol can be affected by tuning the redox potential of the catalyst.

4.2. Influence of Alkali Metal Cation on Catalytic Activity of Encapsulated Complexes. One of the main features of Faujasite-type Y zeolites is the charge-compensating alkali/alkaline-earth metal ions that occupy the three types of positions I, II, and III (NaY with a Si/Al ratio of 2.4 has 55 metal ions per unit cell). Type I metal ions are generally too deeply buried within the sodalite cages to interact with the guest molecule; thus, only type II and type III metal ions are readily accessible. The metal ions are hydrated under ambient conditions, and the water molecules are generally located in the cages, cavities, and channels of the zeolite. When the water is removed at elevated temperature, organic guest molecules may be caged within these voids and the metal ions abandon their original position to bind with the organic occupant. The binding interaction depends on the charge density of the metal ion (i.e., the higher its charge density, the stronger the binding).[72]

The size of the alkali metal cation influences the catalytic properties of the encapsulated complexes mainly in three ways: (i) The first is the interaction of the alkali metal cation with the phenyl ring of the 2-napthol. The ability of cations to interact with π-systems, especially phenyl rings, has been implicated in a number of important processes[73]and is recognized as a powerful conformation-controlling tool in synthetic organic chemistry (e.g., use of Na^+ cation in NaY zeolite as conformational recognition sites for chemoselective hydroperoxidation of alkenylarenes[74] or as activation sites for aldehyde derivatives[75]) due to its strength which is several times greater than other interactions, such as hydrogen bonding and van der Waals force. Very recently, Yamashita et al.[76] have reported the predominance of cation$-\pi$ interactions on the significant enhancement of catalytic oxidation of cyclohexene catalyzed by various alkali metal cation functionalized titanosilicate molecular sieves. To clarify the intricate cation$-$guest interaction we carried out DFT calculation at the VWN/DN level and find out the interaction energy. It has been found that the interaction energy decreases as the size of the cation increases, i.e., K^+-2-napthol ($-$24.18 kcal/mol) < Na^+-2-napthol ($-$31.93 kcal/mol) < Li^+-2-napthol ($-$42.45 kcal/mol). On the basis of this we also calculate the adsorption energy ($-\Delta H_{ads}$) from the total energy of a supramolecular system consisting of 2-napthol, an alkali

dx.doi.org/10.1021/ic201959g | *Inorg. Chem.* 2012, 51, 1657−1674

metal cation (herein we consider only Li^+ and K^+), and the zeolite framework. We found that the adsorption energy in the case of K^+-exchanged zeoliteY (39.17 kcal/mol) is less in comparison to the Li^+-exchanged zeolite (42.35 kcal/mol). Moreover, it can be seen from Figure 15 that the HOMO is

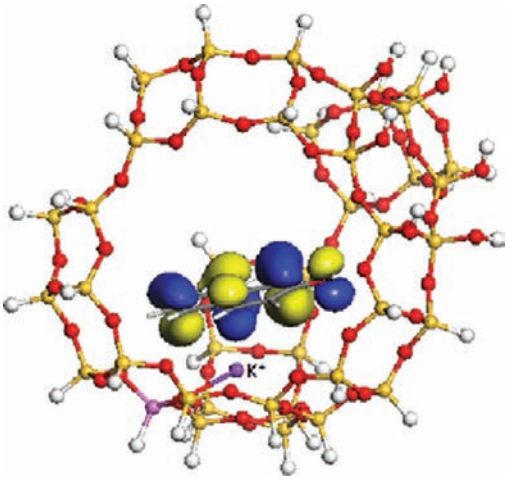

Figure 15. Positions of HOMO orbital in a supramolecular system consisting of a alkali metal cation (K^+), 2-napthol, and the zeolite framework.

fully concentrated on the phenyl ring of 2-napthol and no overlapping occurs between orbital of the caton, K^+. This suggests that the 2-napthol is stabilized within the zeolite cages in the presence of the alkali cation via the electrostatic interactions. On the basis of the experimental and computational results, we can attribute the enhancement of catalytic activity to weak cation−π interactions between heavier alkali metal cations and adjacent 2-napthol molecules which improves the ability of napthol molecules to diffuse within the micropores; contrarily, lighter alkali metal cations hinder the diffusion due to a strong cation−π interaction. (ii) Second, it influences the redox properties of the encapsulated complexes which in turn influence the approach of molecular oxygen and consequently its reduction. (ii) Lastly, the size of the metal cation influences the extent of asymmetric induction in the oxidative coupling of 2-napthol to BINOL. Although all the encapsulated complexes show higher selectivity toward the *R*-conformation, still the size of the alkali cations affects the percentage yield as well as induces chiralty in the resultant product and is found to be highest in the KY zeolite. This may be attributed to the available space in the zeolite supercage for the reactant molecule such that a smaller metal ion suffices. This stereoselectivity behavior is a reflection of the spatial confinement imposed on the guest molecule within the zeolite supercage which forces the complexes to attain stepped conformation once the complex gets oxidized by molecular oxygen. The other way one can describe it is that the larger the size of the alkali metal, the tighter the fit, and the higher the asymmetric induction.

The encapsulated metal complexes show many advantages over their homogeneous counterparts. First, the catalytic activities of Fe-Schiff-base complexes are found to be better than those of their respective nonencapsulated complexes (Table 10). Second, the pure complex dimerizes as it changes color form dark brown to purple-black. This may be attributed to the irreversible deactivation due to the formation of μ-oxo dimeric product, especially in the presence of the oxidant. On the other hand, zeolite encapsulated metal complexes do not undergo any color change during the reaction and could be easily separated and reused. Further, the time required for the conversion of β-napthol to BINOL is significantly less in the presence of the encapsulated metal complexes. Also, we have been successful in reducing the time consumed for such catalytic conversion in contrast to the recent publication dealing with oxidative coupling of 2-napthol.[27,28,77] As illustrated in Table 10, the potassium exchanged zeolites show better activity in comparison to the other catalysts.

5. CONCLUSION

Two monomeric iron(III) complexes of the ligands *N*,*N*′-bis(salicylidene) ethylenediamine (Salen) and *N*,*N*′-disalicylidene-1,2-phenylendiamine (Salophen) with pseudo-square-pyramidal geometry are being synthesized inside the supercase of zeolite Y possessing various extraframework alkali metal cations (Li^+, Na^+, and K^+) via a flexible ligand method. The influence of the alkali metal cations on the electronic transitions, redox, and catalytic abilities of the guest Fe(III) Schiff-base complexes in the restricted void space are investigated. The size of the exchangeable countercation on zeolite framework is found to have profound influence on the LMCT and the average reduction potential of the encapsulated iron complexes. The increase in size of the alkali metal cation from Li^+ to K^+ dramatically red-shifted the lower and the higher energy UV−vis bands. The smaller alkali metal cation interacts more strongly and hinders the passage of 2-napthol into the zeolite matrix. In contrast, presence of the larger cations with high electropositivity and less cation−π interaction energy and donor ability favors the high diffusibility of the incoming guest, influences the redox potential of the guest molecule, and thereby enhances the rate of the catalytic conversion of 2-napthol to BINOL. The Fe-Schiff-base complexes encapsulated in zeolite KY are found to have more negative reduction potential, and hence, varying the alkali metal cations from Li^+ to K^+ results in the enhancement of the catalytic ability of the encapsulated complexes for oxidative coupling of 2-napthol in the presence of molecular oxygen as oxidant. DFT based calculation further supports the enhancement of reactivity on the basis of the change in the global hardness and softness of the systems on encapsulation into zeolite-Y. The catalytic conversion of 2-napthol to BINOL is found to be greater in comparison to the neat complexes, and most importantly, the time required for such conversion is much less than those reported in recently published literature. Moreover, the selectivity toward *R*-configuration is found to be greater in the catalytic conversion of 2-napthol to BINOL in the presence of all the hybrid catalyst.

■ ASSOCIATED CONTENT

Ⓢ Supporting Information

This material is available free of charge via the Internet at http://pubs.acs.org.

■ AUTHOR INFORMATION

Corresponding Author

*E-mail: ramesh@tezu.ernet.in.

■ ACKNOWLEDGMENTS

The authors thank the Department of Science and Technology, New Delhi for financial support.

REFERENCES

(1) (a) Balkus, K. J. Jr.; Gabrielov., A. G. *J. Inclusion Phenom. Mol. Recognit. Chem.* **1995**, *21*, 159−184. (b) De Vos, D. E.; Knops-Gerrits, P.-P.; Parton, R. F.; Weckhuyysen, B. M.; Jacobs, P. A.; Schoonheydt, R. A. *J. Inclusion Phenom. Mol. Recognit. Chem.* **1995**, *21*, 185−213. (c) Dutta, P. K. *J. Inclusion Phenom. Mol. Recognit. Chem.* **1995**, *21*, 215−237. (d) Xuereb, D. J.; Raja, R. *Catal. Sci. Technol.* **2011**, *1*, 517−534. (e) Jacob, C. R.; Varkey, S. P.; Ratnasamy, P. *Appl. Catal., A* **1999**, *182*, 91−96.

(2) Cano, M. L.; Corma, A.; Fornés, V.; García, H.; Miranda, M. A.; Baerlocher, C.; Lengauer, C. *J. Am. Chem. Soc.* **1996**, *118*, 11006−11013.

(3) Álvaro, M.; Cabeza, J. F.; Corma, A.; García, H.; Peris, E. *J. Am. Chem. Soc.* **2007**, *129*, 8074−8075.

(4) Mizuno, K.; Lunsford, J. H. *Inorg. Chem.* **1983**, *22*, 3484−3486.

(5) Bania, K. K.; Deka, R. C. *J. Phys. Chem. C* **2011**, *115*, 9601−9607.

(6) (a) Mortier, W. J.; Schoonheydt, R. A. *Prog. Solid State Chem.* **1985**, *16*, 1−125. (b) Mortier, W. J. *J. Catal.* **1978**, *55*, 138−145. (c) Heidler, R.; Janssens, G. O. A.; Mortier, W. J.; Schoonheydt, R. A. *J. Phys. Chem.* **1996**, *100*, 19728−19734. (d) van Genechten, K. A.; Mortier, W. J. *Zeolites* **1988**, *8*, 273−283.

(7) No, K. T.; Chon, H.; Ree, T.; Jhon, M. S. *J. Phys. Chem.* **1981**, *85*, 2065−2070.

(8) Yashima, T.; Sato, K.; Hayasaka, T.; Hara, N. *J. Catal.* **1972**, *26*, 303−312.

(9) (a) Hattori, H. *Chem. Rev.* **1995**, *95*, 537−550. (b) Tanabe, K.; Misono, M.; Ono, Y.; Hattori, H. *Stud. Surf. Sci. Catal.* **1989**, *51*, 5−25.

(10) Deka, R. C.; Vetrivel, R. *J. Catal.* **1998**, *74*, 88−97.

(11) Deka, R. C.; Roy, R. K.; Hirao, K. *Chem. Phys. Lett.* **2004**, *389*, 186−190.

(12) Mori, K.; Kawashima, M.; Kagohara, K.; Hiromi Yamashita, H. *J. Phys. Chem. C* **2008**, *112*, 19449−19455.

(13) Mori, K.; Kawashima, M.; Kagohara, K.; Hiromi Yamashita, H. *J. Phys. Chem. C* **2008**, *112*, 2593−2600.

(14) Corrêa, R. J.; Salomão, G. C.; Olsen, M. H. N.; Filho, L. C.; Drago, V.; Fernandes, C.; Antunes, O. A. C. *Appl. Catal., A* **2008**, *336*, 35−39.

(15) Poltowicz, J.; Pamin, K.; Tabor, E.; Haber, J.; Adamski, A.; Sojka, Z. *Appl. Catal., A* **2006**, *299*, 235−242.

(16) Sabater, M. J.; Corma, A.; Domenech, A.; Fornes, V.; García, H. *Chem. Commun.* **1997**, *14*, 1285−1286.

(17) Gigante, B.; A. Corma, A.; García, H.; Sabater, M. J. *Catal. Lett.* **2000**, *68*, 113−119.

(18) Jin, C.; Fan, W.; Jia, Y.; Fan, B.; Ma, J.; Li, R. *J. Mol. Catal. A: Chem.* **2006**, *249*, 23−30.

(19) Saha, P. K.; Dutta, B.; Jana, S.; Bera, R.; Saha, S.; Okamoto, K.; Koner, S. *Polyhedron* **2007**, *26*, 563−571.

(20) Knops-Gerrits, P.; De Vos, D. E.; Jacobs, P. A. *J. Mol. Catal. A: Chem.* **1997**, *117*, 57−70.

(21) Mahdavi, V.; Mardani, M.; Malekhosseini, M. *Catal. Commun.* **2008**, *9*, 2201−2204.

(22) Silva, M.; Freire, C.; De Castro, B.; Figueiredo, J. L. *J. Mol. Catal. A: Chem.* **2006**, *258*, 327−333.

(23) Medina, J. C.; Gabriunas, N.; Páez-Mozo, E . *J. Mol. Catal. A: Chem.* **1997**, *115*, 233−239.

(24) Zsigmond, Á.; Horváth, A. A.; Notheisz, J. *J. Mol. Catal. A: Chem.* **2001**, *171*, 95−102.

(25) Haber, J.; Pamin, K.; Poltowicz, J. *J. Mol. Catal. A: Chem.* **2004**, *224*, 153−159.

(26) Zhang, R.; Mab, J.; Wang, W.; Wangc, B.; Li, R. *J. Electroanal. Chem.* **2010**, *643*, 31−38.

(27) Egami, H.; Katsuki, T. *J. Am. Chem. Soc.* **2009**, *131*, 6082−6083.

(28) Egami, H.; Matsumoto, K.; Oguma, T.; Kunisu, T.; Katsuki, T. *J. Am. Chem. Soc.* **2010**, *132*, 13633−13635.

(29) Sinclair, P. E.; Catlow, C. R. A. *J. Phys. Chem. B* **1999**, *103*, 1084−1095.

(30) Hecht, H. G. In *Modern Aspect of Reflectance Spectroscopy*; Wendlandt, W. W., Ed.; Plenum Press: New York, 1968.

(31) Vogel, A. I. *Textbook of Quantitative Chemical Analysis*, 6th ed.; Pearson Education: Beijing, 2002, p 394.

(32) Delly, B. *J. Chem. Phys.* **1990**, *92*, 508−514.

(33) Yang, W.; Mortier, W. J. *J. Am. Chem. Soc.* **1986**, *108*, 5708−5711.

(34) (a) Quayle, W. H.; Lunsford, J. H. *Inorg. Chem.* **1982**, *21*, 97−103. (b) Quayle, W. H.; Peeters, G.; DeRoy, G. L.; Vansant, E. F.; Lunsford, J. H. *Inorg. Chem.* **1982**, *21*, 2226−2231.

(35) Jin, C.; Fan, W. B.; Jia, Y. J.; Fan, B. B.; Ma, J. H.; Li, R. F. *J. Mol. Catal. A: Chem.* **2006**, *249*, 23−30.

(36) Ganesan, R.; Viswanathan, B. *J. Phys. Chem. B* **2004**, *108*, 7102−7114.

(37) Gaber, B. P.; Miskowski, V.; Spiro, T. G. *J. Am. Chem. Soc.* **1974**, *96*, 6868−6873.

(38) Hensen, E. J. M.; Zhu, Q.; Janssen, R. A. J.; Magusin, P. C. M. M.; Kooyman, P. J.; van Santen, R. A. *J. Catal.* **2005**, *233*, 123−135.

(39) Santhosh Kumar, M.; Schwidder, M.; Grünert, W.; Bentrup, U.; Brückner, A. *J. Catal.* **2006**, *239*, 173−186.

(40) Li, L.; Shen, Q.; Li, J.; Hao, Z.; Xu, Z. P.; Lu, G. Q. M. *Appl. Catal., A* **2008**, *344*, 131−141.

(41) Park, Y. S.; Um, S. Y.; Yoon, K. B.; Yoon., K. B. *J. Am. Chem. Soc.* **1999**, *121*, 3193−3200.

(42) Webb, J. In *Techniques and Topics in Bioinorganic Chemistry*; McAuliffe., C. A. Ed.; Wiley: New York, 1975.

(43) Murray, K. S.; Newman, P. S.; Gatehouse.; M., B.; Taylor, D. *Aust. J. Chem.* **1978**, *31*, 983−992.

(44) Shaw, B. R.; Creasy, K. E.; Lanczycki, C. J.; Sargeant, J. A.; Tirhado, M. *J. Electrochem. Soc.* **1988**, *135*, 869−876.

(45) Bessel, C. A.; Rolison, D. R. *Stud. Surf. Sci. Catal.* **1995**, *98*, 114−115.

(46) Cassidy, J.; Breen, W.; O'Donoghue, E.; Lyons, M. E. G. *Electrochim. Acta* **1991**, *36*, 383−384.

(47) Bedioui, F.; Roué, L.; Briot, E.; Devynck, J.; Bell, S. L.; Balkus, K. J. Jr. *J. Electroanal. Chem.* **1994**, *373*, 19−29.

(48) Mesfar, K.; Carre, B.; Bedioui, F.; Devynck, J. *J. Mater Chem.* **1993**, *3*, 873−876.

(49) Bedioui, F.; Deboysson, E.; Balkus, J. Jr.; Devynck, J. *J. Electroanal. Chem.* **1991**, *315*, 313−318.

(50) Bedioui, F.; Boysson, E. D.; Devynck, J.; Balkus, K. J. Jr. *J. Chem. Soc., Faraday Trans.* **1991**, *87*, 3831−3834.

(51) Gaillon, L.; Sajot, N.; Bedioui, F.; Devynck, J.; Balkus, K. J. Jr. *J. Electroanal. Chem.* **1993**, *345*, 157−167.

(52) Bedioui, F.; Roue, L.; Briot, E.; Devynck, J.; Bell, S.; Balkus, K. J. Jr. *J. Electroanal. Chem.* **1994**, *373*, 19−29.

(53) Gemborys, H. A.; Shaw, B. R. *J. Electroanal. Chem.* **1986**, *208*, 95−107.

(54) Shaw, B. R.; Creasy, K. E. *J. Electroanal. Chem. Interfacial Electrochem.* **1988**, *243*, 209−217.

(55) Rolison, D. R. *Chem. Rev.* **1990**, *90*, 867−878.

(56) Baker, M. D.; Seneratne, C.; Zhang, J. *J. Phys. Chem.* **1994**, *98*, 1668−1673.

(57) Calzaferri, G.; Lanz, M.; Li, J. W. *J. Chem. Soc., Chem. Commun.* **1995**, *13*, 1313−1314.

(58) Gerloch, M.; Lewis, J.; Mabbs, F. E.; Richards, A. *Nature* **1996**, *212*, 809−810.

(59) Gerloch, M.; Mabbs, F. E. *J. Chem. Soc. A* **1967**, *14*, 1900−1908.

(60) Parr, R. G.; Chattaraj, P. K. *J. Am. Chem. Soc.* **1991**, *113*, 1854−1855.

(61) Chattaraj, P. K.; Liu, G. H.; Parr, R. G. *Chem. Phys. Lett.* **1995**, *237*, 171−176.

(62) (a) Pearson, R. G. *Chemical Hardness: Applications from Molecules to Solids*; Wiley-VCH Verlag GMBH: Weinheim, 1997. (b) Pearson, R. G. *J. Chem. Educ.* **1987**, *64*, 561−567; *Acc. Chem. Res.* **1993**, *26*, 250−255. (c) Parr, R. G.; Chattaraj, P. K. *J. Am. Chem. Soc.* **1991**, *113*, 1854−1855. Chattaraj, P. K.; Liu, G. H.; Parr, R. G. *Chem. Phys. Lett.* **1995**, *237*, 171−176. Chattaraj., P. K. *PINSA-A: Proc. Indian Natl. Sci. Acad., Part A* **1996**, *62*, 513−519. Chattaraj, P. K.; Cedillo, A.; Parr, R. G. *Chem. Phys.* **1996**, *204*, 429−437. Ayers, P. W.; Parr, R. G. *J. Am. Chem. Soc.* **2000**, *122*, 2010−2018.

(63) Nguyen, L. T.; Le, T. N.; De Proft, F.; Chandra, A. K.; Langenaeker, W.; Nguyen, M. T.; Geerlings, P. *J. Am. Chem. Soc.* **1999**, *121*, 5992 and references therein.
(64) Pal, S.; Chandrakumar, K. R. S. *J. Am. Chem. Soc.* **2000**, *122*, 4145 and references therein.
(65) Chattaraj, P. K. *J. Phys. Chem. A* **2001**, *105*, 511−513.
(66) (a) Luo, Z.; Liu, Q.; Gong, L.; Cui, X.; Mi, A.; Jiang, Y. *Angew. Chem., Int. Ed.* **2002**, *41*, 4532−4535. (b) Guo, Q. X.; Wu, Z. J.; Luo, Z. B.; Liu, Q. Z.; Ye, J. L.; Luo, S. W.; Cun, L. F.; Gong, L. Z. *J. Am. Chem. Soc.* **2007**, *129*, 13927−13938.
(67) Somei, H.; Asano, Y.; Yoshida, T.; Takizawa, S.; Yamataka, H.; Sasai, H. *Tetrahedron Lett.* **2004**, *45*, 1841−1844.
(68) Gao, J.; Reibenspies, J. H.; Martell, A. E. *Angew. Chem., Int. Ed.* **2003**, *42*, 6008−6012.
(69) Tada, M.; Taniike, T.; Kantam, L. M.; Iwasawa, Y. *Chem. Commun.* **2004**, *22*, 2542−2543.
(70) Li, X.; Hewgley, J. B.; Mulrooney, C. A.; Yang, J.; Kozlowski, M. C. *J. Org. Chem.* **2003**, *68*, 5500−5511.
(71) Sabarinathan, S.; Vasuki, G.; Rao, S. P. *Eur. J. Chem.* **2010**, *1*, 360−367.
(72) Sivaguru, J.; Saito, H.; Solomon, M. R.; Lakshmi, S.; Kaanumalle, L. S.; Thomas Poon, T.; Jockusch., S.; Adam, W.; Ramamurthy, V.; Inoue, Y.; Turro, N. J. *Photochem. Photobiol.* **2006**, *82*, 123−131.
(73) (a) Ma, J. C.; Dougherty, D. A. *Chem. Rev.* **1997**, *97*, 1303−1324. (b) Dougherty, D. A. *Science* **1996**, *271*, 163−168. (c) Lakshminarasimhan, P.; Sunoj, B. R.; Chandrasekhar, J.; Ramamurthy., V. *J. Am. Chem. Soc.* **2000**, *122*, 4815−4816.
(74) (a) Stratakis, M.; Froudakis, G. *Org. Lett.* **2000**, *2*, 1369−1372. (b) Stratakis, M.; Rabalakos, C.; Mpourmpakis, G.; Froudakis, G. E. *J. Org. Chem.* **2003**, *68*, 2839−2843. (c) Stratakis, M.; Kalaitzakis, D.; Stavroulakis, D.; Kosmas, G.; Tsangarakis, C. *Org. Lett.* **2003**, *5*, 3471−3474.
(75) (a) Okachi, T.; Fujimoto, K.; Onaka, M. *Org. Lett.* **2002**, *4*, 1667−1669. (b) Okachi, T.; Onaka, M. *J. Am. Chem. Soc.* **2004**, *126*, 2306−2307. (c) Imachi, S.; Onaka, M. *Chem. Lett.* **2005**, *34*, 708−709.
(76) Kuwahara, Y.; Nishizawa, K.; Nakajima, T.; Kamegawa, T.; Mori, K.; Yamashita, H. *J. Am. Chem. Soc.* **2011**, *133*, 12462−12465.
(77) Guo, Q.-X.; Wu, Z.-J.; Luo, Z.-B.; Liu, Q.-Z.; Ye, J.-L.; Luo, S.-W.; Cun, L.-F.; Gong, L.-Z. *J. Am. Chem. Soc.* **2007**, *129*, 13927−13938.